AGU PUBLICATIONS

JGR

Journal of Geophysical Research: Oceans

RESEARCH ARTICLE

10.1002/2014JC010589

Key Points:

- Full-polarimetric Doppler signature of the ocean
- Nonlinear sea surface modeling
- Sea surface scattering and Doppler modeling

Correspondence to:
F. Fois,
f.fois@tudelft.nl

Citation:
Fois, F., P. Hoogeboom, F.L. Chevalier, and A. Stoffelen (2015), An analytical model for the description of the full-polarimetric sea surface Doppler signature, *J. Geophys. Res. Oceans*, *120*, 988–1015, doi:10.1002/2014JC010589.

Received 19 NOV 2014
Accepted 14 JAN 2015
Accepted article online 21 JAN 2015
Published online 18 FEB 2015

An analytical model for the description of the full-polarimetric sea surface Doppler signature

Franco Fois[1,2], Peter Hoogeboom[1], François Le Chevalier[3], and Ad Stoffelen[4]

[1]Department of Geoscience and Remote Sensing, Delft University of Technology, Delft, Netherlands, [2]Also at Rhea System, European Space Agency (ESA/ESTEC), Noordwijk, Netherlands, [3]Department of Mathematics and Computer Science, Delft University of Technology, Delft, Netherlands, [4]Royal Netherlands Meteorological Institut, de Bilt, Netherlands

Abstract This paper describes an analytical model of the full-polarimetric sea surface scattering and Doppler signature. The model combines the small-slope-approximation theory (at the second order) with a weak nonlinear sea surface representation. Such a model is used to examine the variation of the Doppler central frequency/bandwidth and of the normalized radar cross section as function of wind speed and direction. The results suggest that the model can be a valuable tool for the accurate observation of sea surface currents.

1. Introduction

Accurate knowledge of spatial and temporal surface current behavior in the open ocean and coastal waters is essential for a variety of applications, such as the monitoring of changes in coastal regions, risk management for coastal and offshore structures, and ship operations. Currents are generated from the forces acting upon the water mass including the rotation of the Earth, winds, temperature and salinity differences, and tidal forces. Additionally, depth contours and the shoreline influence the currents' direction and strength. Use of SAR-derived Doppler observation to estimate surface current in some selected areas of strong persistent current, such as Gulf stream and Agulhas current, has emerged recently [*Chapron et al*., 2003, 2005; *Johannessen et al*., 2008], even if the validation was based on the few opportunities offered by Lagrangian surface drifters of the world ocean drifter program.

Surface currents moreover emerge when long-term differences are taken between scatterometer winds and Numerical Weather Prediction (NWP) model winds, since the satellite scatterometer winds are derived from ocean roughness, which depends on the relative motion difference between air and sea, whereas NWP model winds are provided with respect to a fixed Earth reference. These differences have also been favorably compared to SAR Doppler measurements. Although scatterometer winds are used beneficially for NWP model initialization [*Stoffelen et al*., 2013], it may be clear that for the more successful use of scatterometer winds in NWP analyses, the ocean currents and motion need to be known and taken into account.

The measurement of ocean currents from a satellite in low Earth orbit is difficult due to the very high satellite velocity ($\sim$7 km/s) with respect to that of the ocean current to be measured (from a few cm/s to some m/s). As a consequence, accurate knowledge of the satellite radar beam pointing would be required. An alternative approach for removing the satellite and Earth-rotation components of the observed Doppler velocity would be to make use of some reference surface currents known a priori by independent means such as drifting buoys, current meters, and coastal Doppler radars as well as the landmasses whose earth-relative velocity is zero by definition.

Even if promising methodology has been developed, some intrinsic limitations on the use of SAR Doppler shift for surface current mapping remains, such as the need to rely on a model quantifying the wind contribution to the total Doppler shift.

In fact, one major challenge is that Doppler shift is not only sensitive to the underlying ocean surface current and to satellite orbital position/attitude knowledge errors, but it is also strongly dependent on wind speed and direction. Depending on the wind speed, the Doppler shift induced by the wind (wind drift) could be much higher than the one induced by the current. Improved understanding and modeling of the microwave sea surface Doppler signature thus becomes imperative for accurate determination of ocean currents.

The modeling of the Doppler spectrum of a time-varying ocean surface has gained considerable attention in the last decade. Knowledge of how the evolution of the ocean surface wave spectrum affects the scattered electromagnetic waves is essential for a quantitative understanding of the properties of the measured microwave Doppler spectra. Such an understanding is complex because of the complicated hydrodynamics influencing the motion of the ocean surface waves. Nonlinear hydrodynamics couple the motion of the large and small waves and, in turn, change the shapes and the statistical characteristics of the surface wave components and thus its interaction with the winds. These hydrodynamic surface interactions are not represented in the simplest linear sea surface models, which assume that each surface harmonic propagates according to the dispersion relation of water waves. Among the first meaningful papers, one should mention the early works of *Bass* [1968] and *Barrick and Weber* [1977], who used a surface perturbation theory to predict the Doppler spectra; *Valenzuela and Laing* [1970], instead, obtained similar results by using a composite surface model. Later, Doppler spectra were studied by *Thompson* [1989] and *Romeiser and Thompson* [2000], who computed the spectra using a time-dependent composite model. This model reduces to *specular* and *small-perturbation* limits for VV and HH-polarizations and its time dependence is based on the use of a linear modulation transfer function. *Zavorotny and Voronovich* [1998] made use of an approximate "two-scale" surface model based on a directional wave spectrum, which takes into account the wave age. In *Creamer et al*. [1989], the authors proposed a nonlinear model for the description of hydrodynamic surface interactions which was eventually used by *Rino et al*. [1991] to simulate the Doppler spectra from dynamically evolving surface realizations. However, the simulations were performed with a rather large electromagnetic wavelength (7.5 m) and were restricted to only 70° incidence angle. Later, *Toporkov and Brown* [2000], *Toporkov and Sletten* [2007], *Soriano et al*. [2006], *Li and Xu* [2011], *Johnson et al*. [2001], and *Hayslip et al*. [2003] made significant steps forward in modeling L-band and X-band nonlinear surface scattering properties at low wind speeds. In these works, since no statistical formulation was available, Doppler spectra were generated by averaging the backscattered field from a large number of sampled time-evolving surfaces, a procedure which is very time-consuming. A further difficulty arises from the fact that the Creamer technique is computationally demanding and actually dissuasive for two-dimensional surface simulations. Therefore, most of the studies have been limited to one-dimensional surfaces.

An alternative numerical method for studying the evolution of free and bound waves on the nonlinear ocean surface was proposed by *West et al*. [1987]. Although this method is more efficient than the Creamer technique [*Johnson et al*., 2001], it is susceptible to instability problems and breaks down when steep features in the surface are formed.

Recently, the use of the Choppy Wave Model (CWM) in combination with the weighted curvature approximation [*Nouguier et al*., 2009, 2010, 2011] in the context of sea Doppler spectrum calculation has shown significant advantages in terms of analytical simplicity and numerical efficiency. However, the Weighted Curvature Approximation (WCA) does not provide a full-polarimetric description of the sea surface Doppler signature. In addition, most of the numerical results reported by *Nouguier et al*. [2011] refer only to one-dimensional representations of the sea surface. Although in the last 10 years the modeling of sea surface Doppler signature has made significant progress, an efficient analytical model of the full-polarimetric sea surface Doppler spectrum is still missing. Additionally, not many comparisons with real measurements have been published: among the few attempts one should mention the works by *Plant and Alpers* [1994] and *Mouche et al*. [2008].

In this paper, we present an analytical physical model for accurate estimation of full-polarimetric microwave sea surface scattering and Doppler signatures. This model combines an adequate sea surface description, based on the CWM, with second-order Small-Slope-Approximation (SSA) wave scattering theory to simulate both scattering and Doppler spectra over a wide range of wind speeds, radar frequencies, incidence angles, different polarizations, and arbitrary radar look direction with respect to the wind direction. In section 2, the properties of the ocean sea surface are discussed and differences between linear and nonlinear sea surface representations are presented. Statistical properties of the CWM are also discussed. The section ends with the description of an efficient procedure to undress the sea surface spectrum. Section 3 is dedicated to the description of the scattering model, whereas section 4 highlights the links between the present general analytical model and simplified scattering theories. In section 5, the results are first compared with other scattering theories and then (in section 6) with real measurements from Envisat-ASAR (C-band radar), the well-established Empirical Geophysical Model Function CDOP [*Mouche et al*., 2012], and data collected in Ku-band during the SAXON-FPN campaign [*Plant and Alpers*, 1994; *Plant et al*., 1994].

Being capable of estimating full-polarimetric Doppler spectra of microwave backscatter from ocean surface, this model could be used to explore ocean surface motion retrievals, thus potentially supporting the definition of future scatterometers capable of simultaneous measurement of Ocean Vector Wind (OVW) and Ocean Vector Motion (OVM) on a global scale.

2. Properties of the Ocean Sea Surface

The 2-dimensional properties of the sea surface determine the characteristics of the measured Normalized Radar Cross Section (NRCS). In this section, we focus our attention on the properties of the surface wave spectrum and how they depend on environmental parameters such as the local wind vector. Evaluation of the wave height variance spectrum over the footprint of a microwave radar is extremely challenging. This is not only because of the broad range of roughness scales present on the sea surface, from millimeter wavelengths to wavelengths on the order of hundred meters, but also because no single technique is able to determine wave height variance spectral densities over the entire range of wavelengths: resolution and dynamic range constraints are the main limitations. Most routine measurements of the sea surface are limited to the height and directional characteristics of the wavefield collected from a wave buoy at a single position in space as function of time. Many studies in the recent literature have tried to incorporate such measurements into stationary models for the sea surface wave height variance spectra. These models generally characterize the measured properties of the sea surface through the spectral moments. Today, one of the most well-known and accepted spectral models is the Elfouhaily unified spectrum [*Elfouhaily et al*., 1997]. The development of this spectrum was based on available field and wave-tank measurements along with physical arguments. It is fully consistent with Donelan spectrum [*Donelan and Pierson*, 1987] for the long-wave part, whereas, for the short-wave part, it is consistent with the optical tank measurements by *Jähne and Riemer* [1990]. The reader is referred to the original paper in order to obtain the explicit expression of the wave height variance spectral density. The ocean surface wave spectrum by *Kudryavtsev et al*. [1999] has improved the modeling of short gravity and capillary waves. The spectral shape results from the solution of the energy spectral density balance equation. In the original paper, Kudryavtsev demonstrated that the measured statistical properties of the sea surface (related to the short waves), their wind speed dependence and angular spreading, and the wind speed dependence of integral mean square slope and skewness parameters are well reproduced by the model. Across this paper, also other well-known ocean surface wave vector spectra will be analyzed and their effect on both NRCS and Doppler shift will be addressed; among them, the Apel composite wideband spectrum [*Apel*, 1994], the Pierson-Moskowitz spectrum [*Pierson and Moskowitz*, 1964] and the advanced roughness spectrum by *Hwang et al*. [2011]. Very often, the ocean sea surface is represented by a Gaussian wave height distribution: this is also called linear sea surface model, which assumes that each surface harmonic propagates according to the dispersion relation typical of water waves. However, nonlinear surface waves can have an important impact on the interpretation of scattering data and cannot be ignored for a correct estimation of the sea surface Doppler shift. Nonlinear hydrodynamic modulation of short waves by large waves changes the statistics of the sea surface waves and it is one of the reasons for the observed upwind/downwind asymmetry of the measured NRCS. The deviation from the Gaussian law of the sea surface slope distribution has been well documented since the pioneering work by *Cox and Munk* [1954]. One should also mention the early works of *Hasselmann* [1962] and *Longuet-Higgins* [1963]; however, these theories are only applicable to long gravity waves. For short waves, instead, nonlinear wave-wave interactions become important and must be accounted for: a way of doing this is to use the nonlinear model for surface waves by *Creamer et al*. [1989]. This theory captures the lowest-order nonlinear behavior of surface waves, but lacks a statistical formulation and the numerical implementation of this theory is highly time-consuming and actually dissuasive for 2-D (two-dimensional) surfaces simulations. A numerically efficient weakly nonlinear model, called "Choppy Wave Model" (CWM) has been recently developed to overcome these main limitations [*Nouguier et al.*, 2009]. The CWM is based on a nonlinear transformation of the linear surface and it allows a statistical formulation of the surface height/slopes and higher-order moments. The CWM is limited to the lowest-order nonlinearity. Its main strength is to provide a good compromise between simplicity, stability, and accuracy. Because of these desirable features, the Choppy wave model will be adopted in this paper.

2.1. Linear Sea Surface Model

Without loss of generality we can express the linear sea surface in time as

$$h(\mathbf{r},t)=\int d\mathbf{k}[\hat{h}(\mathbf{k})\exp(-i\omega_{\mathbf{k}}t)+\hat{h}^{*}(-\mathbf{k})\exp(i\omega_{\mathbf{k}}t)]e^{i\mathbf{k}\cdot\mathbf{r}}, \tag{1}$$

where $\hat{h}(\mathbf{k})$ is the complex amplitude of the wave, $\mathbf{r}=(x,y)$ is the horizontal coordinate, $\mathbf{k}$ is the corresponding wave number of polar coordinates (k,φ), and $\omega_{\mathbf{k}}$ is the gravity-capillary dispersion relationship for infinite-depth sea

$$\omega_{\mathbf{k}}=\sqrt{g|\mathbf{k}|\left[1+\left(\frac{|\mathbf{k}|}{k_M}\right)^2\right]}, \tag{2}$$

with $k_M=363.2$ rad/m being the wave number with minimum phase speed and $g=9.81$ m/s^2 the gravity acceleration constant. Denoting with $C(\mathbf{r},t)=\langle h(\mathbf{r},t)h(\mathbf{0},0)\rangle$ the spatiotemporal covariance function of the surface, that is,

$$C(\mathbf{r},t)=\int d\mathbf{k}[S_a(\mathbf{k})\exp(-i\omega_{\mathbf{k}}t)+S_a(-\mathbf{k})\exp(i\omega_{\mathbf{k}}t)]e^{i\mathbf{k}\cdot\mathbf{r}}, \tag{3}$$

where

$$\begin{cases} S_a(\mathbf{k})=S(\mathbf{k})\cos^2\left(\dfrac{\phi-\phi_w}{2}\right) \\ S_a(-\mathbf{k})=S(\mathbf{k})\sin^2\left(\dfrac{\phi-\phi_w}{2}\right) \end{cases}. \tag{4}$$

In (4), $S(\mathbf{k})$ is the centrosymmetric wave spectrum and the angle ϕ_w is the wind direction.

2.2. Nonlinear Sea Surface Model

As a nonlinear representation of the sea surface, we will use the CWM that is based on a Lagrangian approach and takes into account the horizontal displacement of particles. Practically, the nonlinear surface can be expressed as a horizontal deformation of the linear surface as follows:

$$(\mathbf{r},h(\mathbf{r},t))\rightarrow(\tilde{\mathbf{r}},\tilde{h}(\tilde{\mathbf{r}},t)), \tag{5}$$

where

$$\begin{cases} \tilde{\mathbf{r}}=\mathbf{r}+\mathbf{D}(\mathbf{r},t) \\ \tilde{h}(\tilde{\mathbf{r}},t)=h(\mathbf{r},t) \end{cases}. \tag{6}$$

The displacement $\mathbf{D}$ is the so-called Riesz transform of the function h

$$\mathbf{D}(\mathbf{r},t)=\int d\mathbf{k}\, i\frac{\mathbf{k}}{k}e^{i\mathbf{k}\cdot\mathbf{r}}\hat{h}(\mathbf{k},t), \tag{7}$$

and

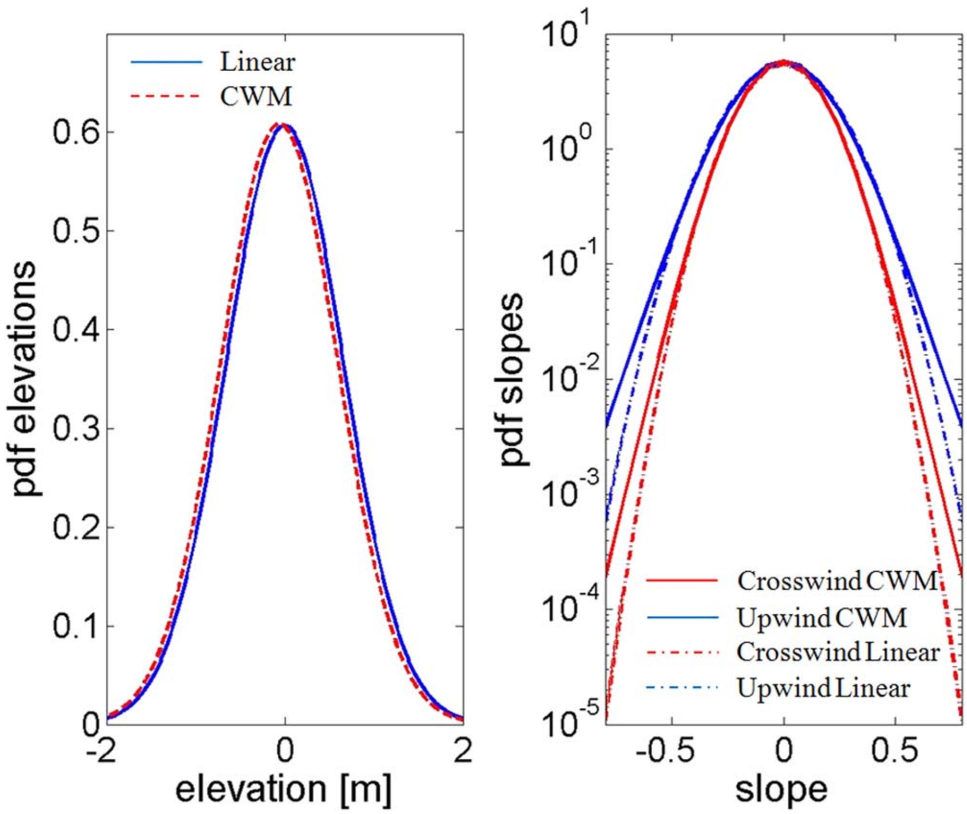

Figure 1. (left) Distribution of elevations and (right) distribution of slopes for linear and CWM surfaces at wind speed of 10 m/s.

$$\hat{h}(\mathbf{k},t)=\frac{1}{(2\pi)^2}\int d\mathbf{r}e^{-i\mathbf{k}\cdot\mathbf{r}}h(\mathbf{r},t) \tag{8}$$

is the two-dimensional spatial transform of the linear surface. The transformation (6) defines a modified process $\tilde{h}(\tilde{\mathbf{r}},t)$ which has been shown to possess non-Gaussian height and slope distributions, as well as a modified spectrum [*Nouguier et al.*, 2009].

2.3. Statistical Properties of the Sea Surface Model

Following the example of *Nouguier et al*. [2009], this section shortly recalls the spatial statistical properties of the nonlinear sea surface, $\tilde{h}$, at a given time $t=0$. Let us introduce the partial and total absolute moments of the spectrum

$$\sigma^2_{\alpha\beta\gamma}=\int\frac{{k_x}^{\alpha}{k_y}^{\beta}}{|\mathbf{k}|^{\gamma}}S(\mathbf{k})d\mathbf{k}, \quad \sigma_n^2=\int|\mathbf{k}|^nS(\mathbf{k})d\mathbf{k}, \tag{9}$$

where k_x and k_y are the components of **k** along the x and y axis. Using the same notation as in *Nouguier et al*. [2009], the characteristic function of the nonlinear surface is given by

$$\Phi(v)=<e^{iv\tilde{h}}>=(1-iv\sigma_1^2+v^2\Sigma_1)\exp\left(-\frac{1}{2}v^2\sigma_0^2\right), \tag{10}$$

with $\Sigma_1=\sigma^4_{111}-\sigma^2_{201}\sigma^2_{021}$. A Fourier inversion of (10) provides the probability distribution function (pdf) of elevations

$$\tilde{P}_0(z)=P_0(z)\left(1+\frac{\Sigma_1}{\sigma_0^2}-\frac{\sigma_1^2}{\sigma_0^2}z-\frac{\Sigma_1}{\sigma_0^4}z^2\right), \tag{11}$$

being $P_0(z)$ a Gaussian distribution of elevations with standard deviation σ_n and zero mean value. Starting with a zero mean linear surface, the resulting nonlinear surface becomes a nonzero mean random non-

Table 1. Statistics of Linear and CWM Surfaces

Wind Speed (m/s)	SURFACE	Root Mean Square HEIGHT (M)	Slope Upwind	Slope Crosswind
5	Linear	0.1625	0.1369	0.1120
5	CWM	0.1628	0.1382	0.1129
7	Linear	0.3195	0.1516	0.1255
7	CWM	0.3201	0.1533	0.1266
10	Linear	0.6573	0.1870	0.1562
10	CWM	0.6586	0.1902	0.1585
12	Linear	0.9481	0.2035	0.1693
12	CWM	0.9498	0.2076	0.1723

Gaussian process. An expression of the slopes of the nonlinear surface can be obtained by differentiating equation (6). An integral formula providing the pdf of slopes has been provided in *Nouguier et al.* [2009, equation (47)]. Figure 1 shows the pdf of elevations (left) and the pdf of slopes (right) of a linear and CWM surfaces for wind speed of 10 m/s (Elfouhaily spectrum). The skewness of the CWM surface is slightly negative and the mean square height (msh) is slightly decreased. There is no significant creation of kurtosis with respect to the Gaussian case. The tail of the slope distribution of the CWM surface shows a slower decrease than the one of the linear surface. Statistics of the linear and nonlinear sea surface are summarized in Table 1: this table highlights a magnification of the rms slopes induced by the nonlinear CWM transformation of the sea surface. This magnification may generate small errors in the estimation of the radar cross section. A way to correct this artifact is to undress the nonlinear sea surface spectrum.

2.4. Spectral Undressing

With reference to Figure 2a, we consider the Elfouhaily spectrum as the reference measured sea surface wave height spectrum, $S_{ref}(\mathbf{k})$. Being the result of a measurement, this spectrum already includes nonlinear features. By applying the nonlinear sea surface transformation (6), $S_{ref}(\mathbf{k})$ is changed in $\tilde{S}(\mathbf{k})$, named "dressed" spectrum, which statistical properties are different from the ones of $S_{ref}(\mathbf{k})$. In particular, the dressed spectrum shows an enhanced curvature that needs to be corrected: a way to do this is by "undressing" $\tilde{S}(\mathbf{k})$. We call the "undressed" spectrum, $S(\mathbf{k})$, the spectrum that after CWM transformation provides the same root mean square height and slope as the reference spectrum $S_{ref}(\mathbf{k})$.

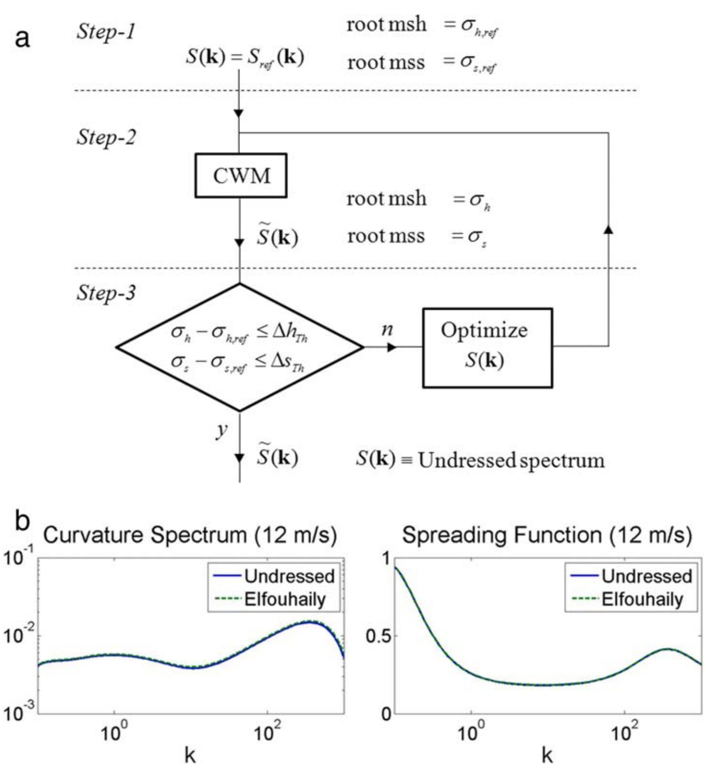

Figure 2. (a) Schematic of the undressing procedure. (b) Comparison between (left) the Elfouhaily and the undressed curvature spectrum and (right) the spreading function for 12 m/s wind speed.

Soriano et al. [2006] proposed a simple undressing method based on an optimization of the high-frequency part of the spectrum. *Nouguier et al.* [2009, 2010] used the iterative procedure proposed by *Elfouhaily et al.* [1999] to perform the undressing. However, not many details on the practical implementation were provided in the above mentioned papers.

In this work, we propose an alternative technique that is based on the use of a parametric representation of the directional sea surface spectrum. The parameters are then optimized through an iterative procedure to make both mss (mean square slope) and msh (mean square height) of the parametric spectrum consistent with the mss and msh of the measured spectrum. For each wind speed, we first

Table 2. Root Mean Square of the Undressed Spectrum

Wind Speed (m/s)	Surface	Root Mean Square Height (m)	Slope Upwind	Slope Crosswind
5	Linear	0.1625	0.1369	0.1120
5	Undr. + CWM	0.1625	0.1370	0.1120
7	Linear	0.3195	0.1516	0.1255
7	Undr. + CWM	0.3196	0.1516	0.1254
10	Linear	0.6573	0.1870	0.1562
10	Undr. + CWM	0.6579	0.1874	0.1562
12	Linear	0.9481	0.2035	0.1693
12	Undr. + CWM	0.9490	0.2036	0.1691

represent the sea spectrum as linear combination of seven different directional spectra: *Elfouhaily et al*. [1997], *Kudryavtsev et al*. [1999], *Apel* [1994], *Pierson and Moskowitz* [1964], *Hwang et al*. [2011], *Fung and Lee* [1982], and *Plant* [2002]. The 14 coefficients of the linear combination (seven coefficients for the curvature spectrum and seven for the spreading function) are optimized, for different values of the wind speed, to match as close as possible the root mss and the root msh of the Elfouhaily spectrum. Practically, the calculation of the parameters is performed with the help of the Matlab routine lsqnonlin [*Coleman and Li*, 1996]. A similar optimization procedure has been used efficiently in *Fois et al*. [2014a] to match Ku and C-band experimental normalized radar cross sections.

The advantage of combining existing sea surface spectra is that the solution of the optimization has always a physical meaning. Other approaches based on parametric fitting of the sea surface spectra, instead, very often bring to nonphysical solutions. As a starting point of the optimization, we consider a spectrum identical to the Elfouhaily one; the coefficients of the linear combination are eventually changed to solve a nonlinear least squares problem, so that the nonlinear surfaces possess the same height and slopes root mean squares as the linear Elfouhaily surface. In Table 2, both root mss and root msh of the linear and undressed nonlinear sea surface are compared for different wind speeds.

Figure 2b shows the undressed spectrum against the Elfouhaily spectrum for 12 m/s wind speed: both curvature spectra and spreading functions are plotted. For the spreading function, we have limited our study to spectra with second harmonic. From our analysis, the undressing procedure was found to have very little impact on the Doppler signature. Therefore, for the specific purpose of Doppler analysis, such a complicated spectral correction can be avoided.

2.5. Scattering Model

An example of an advanced backscattering model for the ocean surface is the *Kirchhoff approximation* model (KA) [*Beckmann and Spizzichino*, 1987], which can only be applied to surfaces with horizontal roughness scale and average radius of curvature (r_c) larger than the electromagnetic wavelength, that is,

$$r_c \cdot k\cos^3\theta_i \gg 1, \tag{12}$$

where θ_i is the incidence angle. The formulation of the Kirchhoff approximation is based upon the Green's theorem, which states that the scattered field at any point within a source free region, bounded by a closed surface, can be expressed in terms of tangential fields on the surface. The Kirchhoff approximation correctly models quasi-specular scattering, but disregards polarization. The KA model is exact when the signal wavelength tends to zero (*geometrical optics* limit, GO), if multiple reflections/shadowing can be neglected. When both the standard deviation and correlation length of surface heights are smaller than the wavelength, a different method must be used. One standard approach is the *small-perturbation method* (SPM) [*Ulaby et al*., 1990], which requires the standard deviation of heights (σ) to be less than about 5% of the electromagnetic wavelength. In addition to the standard deviation requirement, the average slope of the surface should be of the same order of magnitude as the wave number times the standard deviation of heights, mathematically,

$$\begin{cases} k\sigma < 0.3 \\ \sqrt{2}\sigma/l < 0.3 \end{cases}, \tag{13}$$

being l the correlation length of the surface (for power law type of spectra, typical of sea surface, is not easy to define unambiguously l). The SPM yields the proper polarization sensitivity, but does not account for long-scale features in the surface spectrum and does not account for specular scattering either.

KA and SPM involve two special types of rough surfaces: the surface roughness has to be either large or small, compared with the incidence wavelength. Natural surfaces, however, may include both types of roughness in

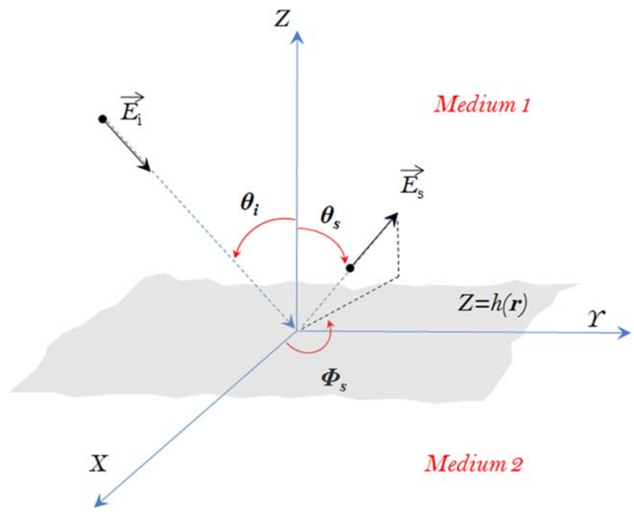

Figure 3. Geometry of surface scattering problem.

various proportions. Some surfaces may have one continuous distribution of roughness instead of two significantly different average sizes. For two-scale surfaces, a simple approximate treatment of this two-scale surface problem is possible. The combination of GO, for small incidence angles, and SPM, for incidence angles above 20°, is called *two-scale model* (TSM) [*Wright*, 1968]. The main weakness of the classical TSM is the arbitrariness of the separation scale between small and large waves. The two-scale model is unable to correctly predict the cross-polar signal in the plane of incidence, and it sensibly underestimates the scattering at large incidence angles. Models which do not have the above mentioned drawback are called unified scattering models. They, in fact, replace the two-scale description of the scattering process with a unique expression of the scattering amplitude with a smooth transition from GO-regime to SPM-regime. Among these models, we mention the *small slope approximation* (SSA) [*Voronovich*, 1994], which, in principle, can be applied to any wavelength, provided that the tangent of grazing angles of incident/scattered radiation sufficiently exceeds the rms slope of roughness. For a sea surface, the slopes are generally small except for steep breaking waves, which represent a relatively small percentage and occur only at strong and very strong wind speeds. The small-slope-approximation is the result of a Taylor expansion with respect to the powers of surface slopes. It is common practice to call SSA1 and SSA2 the expansion performed at the first and second order, respectively, the second being able to estimate the cross-polarized component of scattering in the plane of incidence. Another unified scattering model is the *weighted curvature approximation* (WCA) [*Elfouhaily et al*., 2003]. It is more accurate than the SSA1 and can work at larger incidence angles; in particular, it improves the horizontal polarization estimation. Being a single scattering theory, as for the KA and SSA1, the WCA predicts null cross-polarization in the plane of incidence. In this paper, we will refer to the second-order small-slope-approximation model, SSA2, being the only model able to provide accurate full-polarimetric sea surface scattering signatures [*Fois et al*., 2014b].

2.6. Scattering Geometry, Notations, and Definitions

Let us choose the right Cartesian coordinate system as depicted in Figure 3. The sea surface $z=h(\mathbf{r})$, with $\mathbf{r}=x\hat{\mathbf{x}}+y\hat{\mathbf{y}}$, separates two homogeneous half-spaces with permittivities ε_1 (upper half-space, $z>0$) and ε_2 (lower half-space, $z<0$). In the following, we will consider waves of frequency ω and the time dependence exp $[-i\omega t]$ will be omitted. The rough sea surface is illuminated by a plane monochromatic e.m. wave, coming from the upper half-space, impinging on the surface at incidence angle θ_i. The incident direction is defined by the wave vector $\mathbf{K}_i=\mathbf{k}_i-q_{ki}\hat{\mathbf{z}}$, with $\mathbf{k}_i=k_{ix}\hat{\mathbf{x}}+k_{iy}\hat{\mathbf{y}}$ and $q_{ki}=\sqrt{K_1^2-k_i^2}$, where the wave number K_1 in the upper half-space is given by $K_1=\sqrt{\mu_1\varepsilon_1}2\pi/\lambda$, being λ the wavelength in vacuum. The incident plane wave is given by

$$\mathbf{E}_i=\frac{1}{\sqrt{q_{ki}}}\exp\left(i\mathbf{k}_i\cdot\mathbf{r}-iq_{ki}z\right)\ \mathbf{e}^i_{\alpha_i}(\mathbf{k}_i), \tag{14}$$

where $\mathbf{e}^i_{\alpha_i}(\mathbf{k}_i)$ is the unit vector defining the polarization of the incident plane wave. Here $\alpha_i=1, 2$ is the index describing the vertical and horizontal polarizations of the electromagnetic wave, respectively. In particular, we can express $\mathbf{e}^i_{\alpha_i}(\mathbf{k}_i)$ in the following way:

$$\mathbf{e}^i_1(\mathbf{k}_i)=-\frac{(k_i^2\hat{\mathbf{z}}+q_{ki}\mathbf{k}_i)}{K_1k_i},\quad \mathbf{e}^i_2(\mathbf{k}_i)=\frac{(\hat{\mathbf{z}}\times\mathbf{k}_i)}{k_i}. \tag{15}$$

The incident field $\mathbf{E}_i$ gives rise to a scattered field $\mathbf{E}_s$ in the upper half-space, moving in the direction $\mathbf{K}_s=\mathbf{k}_s+q_{ks}\hat{\mathbf{z}}$, with $\mathbf{k}_s=k_{sx}\hat{\mathbf{x}}+k_{sy}\hat{\mathbf{y}}$ and $q_{ks}=\sqrt{K_1^2-k_s^2}$. Following the Rayleigh decomposition, the scattered field can be written as superposition of outgoing plane waves

$$\mathbf{E}_s = \sum_{\alpha_s=1,2} \int \frac{d\mathbf{k}_s}{\sqrt{q_{ks}}} S_{\alpha_s\alpha_i}(\mathbf{k}_s, \mathbf{k}_i) \exp\left(i\mathbf{k}_s \cdot \mathbf{r} + iq_{ks}z\right) \mathbf{e}^s_{\alpha_s}(\mathbf{k}_s), \tag{16}$$

where $S_{\alpha_s\alpha_i}(\mathbf{k}_s, \mathbf{k}_i)$ is the so-called scattering amplitude (SA) and $\mathbf{e}^s_{\alpha_s}(\mathbf{k}_s)$ is the scattered polarization given, for $\alpha_s = 1, 2$, by

$$\mathbf{e}^s_1(\mathbf{k}_s) = -\frac{(k_s^2\hat{\mathbf{z}} + q_{ks}\mathbf{k}_i)}{K_1 k_s}, \quad \mathbf{e}^s_2(\mathbf{k}_s) = \frac{(\hat{\mathbf{z}} \times \mathbf{k}_s)}{k_s}. \tag{17}$$

With reference to the four polarization coefficients, $\alpha_i = 1, 2$ and $\alpha_s = 1, 2$, the scattering process can be described by the following 2×2 matrix:

$$\mathbf{S}(\mathbf{k}_s, \mathbf{k}_i) = \begin{bmatrix} S_{11}(\mathbf{k}_s, \mathbf{k}_i) & S_{12}(\mathbf{k}_s, \mathbf{k}_i) \\ S_{21}(\mathbf{k}_s, \mathbf{k}_i) & S_{22}(\mathbf{k}_s, \mathbf{k}_i) \end{bmatrix}. \tag{18}$$

Some more quantities must be defined to better describe the scattering from the sea surface, such as the scattered power ensemble averaged moments. The first-order moment, also known as the *coherent scattered amplitude*, is defined as

$$V_{\alpha_s\alpha_i}(\mathbf{k}_s, \mathbf{k}_i) = \langle S_{\alpha_s\alpha_i}(\mathbf{k}_s, \mathbf{k}_i) \rangle. \tag{19}$$

The incoherent second-order moment or *scattering cross section* of the rough surface is

$$\sigma_{\alpha_s\alpha_i}(\mathbf{k}_s, \mathbf{k}_i) = \langle |S_{\alpha_s\alpha_i}(\mathbf{k}_s, \mathbf{k}_i) - \langle S_{\alpha_s\alpha_i}(\mathbf{k}_s, \mathbf{k}_i) \rangle|^2 \rangle. \tag{20}$$

For distributed targets, the common quantity used in remote sensing is the *normalized radar cross section* (NRCS), which is defined as

$$\sigma^0{}_{\alpha_s\alpha_i}(\mathbf{k}_s, \mathbf{k}_i) = \lim_{A\to\infty} \frac{4\pi \langle |S_{\alpha_s\alpha_i}(\mathbf{k}_s, \mathbf{k}_i) - \langle S_{\alpha_s\alpha_i}(\mathbf{k}_s, \mathbf{k}_i) \rangle|^2 \rangle}{A}, \tag{21}$$

where A is the area illuminated by transmit antenna pattern. Only normalized radar cross sections will be reported in this work.

2.7. Second-Order Small-Slope Approximation for a Linear Sea Surface

The computation of SSA2 scattering amplitude is very complicated as it requires the calculation of fourfold integrals with oscillating functions. The SSA2 presents the following expression of the scattering amplitude for a linear sea surface:

$$\mathbf{S}^{SSA-2}_{\alpha_s\alpha_i}(\mathbf{k}_s, \mathbf{k}_i, t)|_{Lin.} = \frac{1}{Q_z} \int \frac{d\mathbf{r}}{(2\pi)^2} \exp\left[-i\mathbf{Q}_H \cdot \mathbf{r} + iQ_z h(\mathbf{r}, t)\right] \times \left[B_{\alpha_s\alpha_i}(\mathbf{k}_s, \mathbf{k}_i) - \frac{i}{4} \int M_{\alpha_s\alpha_i}(\mathbf{k}_s, \mathbf{k}_i, \xi) \hat{h}(\xi, t) e^{i\xi\cdot\mathbf{r}} d\xi\right], \tag{22}$$

where

$$M_{\alpha_s\alpha_i}(\mathbf{k}_s, \mathbf{k}_i, \xi) = B_2(\mathbf{k}_s, \mathbf{k}_i, \mathbf{k}_s - \xi) + B_2(\mathbf{k}_s, \mathbf{k}_i, \mathbf{k}_i + \xi) + 2Q_z B_{\alpha_s\alpha_i}(\mathbf{k}_s, \mathbf{k}_i), \tag{23}$$

and

$$Q_z = q_{ks} + q_{ki}, \quad \mathbf{Q}_H = \mathbf{k}_s - \mathbf{k}_i, \quad Q_H = |\mathbf{k}_s - \mathbf{k}_i|.$$

Values M, B_2 and B are 2×2 matrices; their expressions are given in the Appendix. The second term in the squared parenthesis of equation (22) represents the second-order correction to the SSA1 model. The spatio-temporal covariance function is the limit of the statistical average

$$Cov(\mathbf{k}_s, \mathbf{k}_i; t)|_{Lin.} = \lim_{A\to\infty} \frac{4\pi \langle |\mathbf{S}^{SSA-2}_{\alpha_s\alpha_i}(\mathbf{k}_s, \mathbf{k}_i, t) - \langle \mathbf{S}^{SSA-2}_{\alpha_s\alpha_i}(\mathbf{k}_s, \mathbf{k}_i, t) \rangle|^2 \rangle}{A}, \tag{24}$$

for an infinite illuminated area A. After tedious manipulations, the following expression can be found:

$$Cov(\mathbf{k}_s,\mathbf{k}_i;t)|_{Lin.}=\frac{4\pi}{Q_z^2}\int\frac{d\mathbf{r}}{(2\pi)^2}R_{\alpha_s\alpha_i}(\mathbf{k}_s,\mathbf{k}_i;\mathbf{r},t)\exp\left[-i\mathbf{Q}_H\cdot\mathbf{r}\right], \tag{25}$$

where

$$\begin{aligned}R_{\alpha_s\alpha_i}(\mathbf{k}_s,\mathbf{k}_i;\mathbf{r},t)=&\\ &-e^{-Q_z^2C(0,0)}|B_{\alpha_s\alpha_i}(\mathbf{k}_s,\mathbf{k}_i)-F_{\alpha_s\alpha_i}(\mathbf{k}_s,\mathbf{k}_i;0)|^2+\\ &e^{-Q_z^2(C(0,0)-C(\mathbf{r},t))}\left[\frac{1}{16}\int|M_{\alpha_s\alpha_i}(\mathbf{k}_s,\mathbf{k}_i;\xi)|^2S(\xi,t)e^{i\xi\cdot\mathbf{r}}d\xi+\right.\\ &(B_{\alpha_s\alpha_i}(\mathbf{k}_s,\mathbf{k}_i)-F_{\alpha_s\alpha_i}(\mathbf{k}_s,\mathbf{k}_i;0,t)+F_{\alpha_s\alpha_i}(\mathbf{k}_s,\mathbf{k}_i;\mathbf{r},t))\times\\ &\left.(B_{\alpha_s\alpha_i}(\mathbf{k}_s,\mathbf{k}_i)-F_{\alpha_s\alpha_i}(\mathbf{k}_s,\mathbf{k}_i;0,t)+F_{\alpha_s\alpha_i}(\mathbf{k}_s,\mathbf{k}_i;-\mathbf{r},t))^*\right],\end{aligned} \tag{26}$$

with

$$F_{\alpha_s\alpha_i}(\mathbf{k}_s,\mathbf{k}_i;\mathbf{r},t)=-\frac{Q_z}{4}\int M_{\alpha_s\alpha_i}(\mathbf{k}_s,\mathbf{k}_i;\xi)S(\xi,t)e^{i\xi\cdot\mathbf{r}}d\xi \tag{27}$$

and

$$C(\mathbf{r},t)=\langle h(\mathbf{r},t)h(\mathbf{0},0)\rangle=\int d\xi\ \ S(\xi,t)\exp\left(i\ \ \xi\cdot\mathbf{r}\right), \tag{28}$$

being $S(\xi,t)=S_a(\xi)\exp\left(-i\omega_\xi t\right)+S_a(-\xi)\exp\left(i\omega_\xi t\right)$, the spectrum of roughness. Note that the spatiotemporal covariance function computed at the time $t=0$ provides the Normalized Radar Cross Section (NRCS), that is,

$$Cov(\mathbf{k}_s,\mathbf{k}_i;0)|_{Lin.}=\sigma^0_{\alpha_s\alpha_i}(\mathbf{k}_s,\mathbf{k}_i)|_{Lin.}. \tag{29}$$

The Doppler spectrum is the Fourier transform of the spatiotemporal covariance function

$$S_{Dop}(\omega)|_{Lin.}=\int dt\ \ e^{-i\omega t}Cov(\mathbf{k}_s,\mathbf{k}_i;t)|_{Lin}. \tag{30}$$

and $f=\omega/2\pi$ is the Doppler frequency shift.

2.8. Second-Order Small-Slope Approximation for Nonlinear Sea Surface

We use the Choppy wave model described in section 2.2 as nonlinear sea surface representation. In this case, the SSA2 presents the following expression for the scattering amplitude at the time t:

$$\begin{aligned}\mathbf{S}^{SSA-2}_{\alpha_s\alpha_i}(\mathbf{k}_s,\mathbf{k}_i,t)|_{Non-Lin.}=\tilde{\mathbf{S}}^{SSA-2}_{\alpha_s\alpha_i}(\mathbf{k}_s,\mathbf{k}_i,t)=\frac{1}{Q_z}\int\frac{d\mathbf{r}}{(2\pi)^2}J(\mathbf{r},t)\exp\left[-i\mathbf{Q}_H\cdot(\mathbf{r}+D(\mathbf{r},t))+iQ_zh(\mathbf{r},t)\right]\\ \times\left[B_{\alpha_s\alpha_i}(\mathbf{k}_s,\mathbf{k}_i)-\frac{i}{4}\int M_{\alpha_s\alpha_i}(\mathbf{k}_s,\mathbf{k}_i,\xi)\hat{h}(\xi,t)e^{i\xi\cdot\mathbf{r}}d\xi\right],\end{aligned} \tag{31}$$

where $J(\mathbf{r},t)$ is the Jacobian of the transformation $\mathbf{r}\rightarrow\mathbf{r}+\mathbf{D}(\mathbf{r},t)$

$$J(\mathbf{r},t)=1+\nabla\cdot\mathbf{D}(\mathbf{r},t)+\partial_xD_x(\mathbf{r},t)\partial_yD_y(\mathbf{r},t)-\partial_xD_y(\mathbf{r},t)\partial_yD_x(\mathbf{r},t). \tag{32}$$

By neglecting the quadratic terms in D_x and D_y, we may approximate

$$J(\mathbf{r},t)\approx1+\nabla\cdot\mathbf{D}(\mathbf{r},t). \tag{33}$$

The spatiotemporal covariance function can be written as

$$Cov(\mathbf{k}_s,\mathbf{k}_i;t)|_{Non-Lin.}=\frac{4\pi}{Q_z^2}\int\frac{d\mathbf{r}}{(2\pi)^2}\tilde{R}_{\alpha_s\alpha_i}(\mathbf{k}_s,\mathbf{k}_i;\mathbf{r},t)\exp\left[-i\mathbf{Q}_H\cdot\mathbf{r}\right], \tag{34}$$

where

$$\tilde{R}_{\alpha_s\alpha_i}(\mathbf{k}_s,\mathbf{k}_i;\mathbf{r},t)=-|\chi_{\alpha_s\alpha_i}(\mathbf{k}_s,\mathbf{k}_i;t)|^2+\sum_{n=1}^{4}\sum_{m=1}^{4}\Psi_{\alpha_s\alpha_i}^{(m,n)}(\mathbf{k}_s,\mathbf{k}_i;\mathbf{r},t). \tag{35}$$

The expression of the terms $\Psi_{\alpha_s\alpha_i}^{(m,n)}(\mathbf{k}_s,\mathbf{k}_i;\mathbf{r},t)$ and $\chi_{\alpha_s\alpha_i}(\mathbf{k}_s,\mathbf{k}_i;t)$ are reported in the Appendix.

2.9. Doppler Central Frequency and Doppler Spread

The Doppler central frequency f_D and the Doppler bandwidth B_D can be obtained through the first two moments of the Doppler spectrum

$$f_D=\frac{1}{2\pi}\frac{\int\omega\cdot S_{Dop}(\omega)d\omega}{\int S_{Dop}(\omega)d\omega} \tag{36}$$

and

$$B_D=\sqrt{\frac{1}{(2\pi)^2}\frac{\int\omega^2\cdot S_{Dop}(\omega)d\omega}{\int S_{Dop}(\omega)d\omega}-(f_D)^2}. \tag{37}$$

These quantities can be quickly computed by the model since they do not depend on time. To better clarify, there are two alternative ways to compute f_D and B_D. The first requires the evaluation of the scattering amplitude as function of time: its Fourier transform will then provide the Doppler Spectrum and from this, by using equations (36) and (37), f_D and B_D can be derived. The second approach consists in using the following relationships between Doppler spectrum and the spatiotemporal covariance function:

$$\int\omega\cdot S_{Dop}(\omega)d\omega=-i\frac{\partial Cov}{\partial t}\bigg|_{t=0} \tag{38}$$

and

$$\int\omega^2\cdot S_{Dop}(\omega)d\omega=-\frac{\partial^2 Cov}{\partial t^2}\bigg|_{t=0}. \tag{39}$$

The second approach represents a more direct derivation of the Doppler central frequency and the Doppler spread which does not require the computation of the Doppler spectrum, $S_{Dop}(\omega)$. This computation could be quite time-consuming, particularly at high frequencies (X, Ku, and Ka-bands) where a smaller time step is required to avoid aliasing effects. Through the use of equations (38) and (39), both central Doppler frequency and Doppler spread can be calculated at the same cost as the NRCS.

3. Derivation of Special Scattering Cases

3.1. The Kirchhoff Approximation

Equation (34) provides the complete expression of the spatiotemporal covariance function of the analytical model. From this equation, special scattering cases can be easily derived. For instance, if only the terms $\Psi_{\alpha_s\alpha_i}^{(m,n)}$, with $m=1,2,3,4$ and $n=1$, are considered, we obtain exactly the Kirchhoff Approximation combined with the Choppy Wave Model (KA-CWM), a model that has been widely investigated by *Nouguier et al*. [2009, 2010, 2011]. Thanks to its simplicity, KA-CWM can be used to quickly check the effect of different input wave height spectra on both Doppler shift and Doppler spread. Figure 4 shows f_D and B_D in V-polarization versus incidence angle at X-band at 5, 7, and 9 m/s wind speed (upwind) for linear and CWM surfaces. Because of the use of the Kirchhoff approximation, the results in V and H-polarization are identical. As expected, higher Doppler frequencies are observed when passing to nonlinear surfaces, the increase being more pronounced at high winds. An even more visible impact is observed on the Doppler width, which is found much larger than in the linear case and quasi-insensitive to the incidence angles above 40°, while the linear counterpart falls off rapidly. Both Doppler shift and the Doppler spread change with the wave height spectrum. In Figure 4, four sea surface spectra are analyzed [*Elfouhaily et al*., 1997; *Apel*, 1994; *Pierson and Moskowitz*, 1964; *Hwang et al*., 2011]. The highest Doppler shift and Doppler spread is found

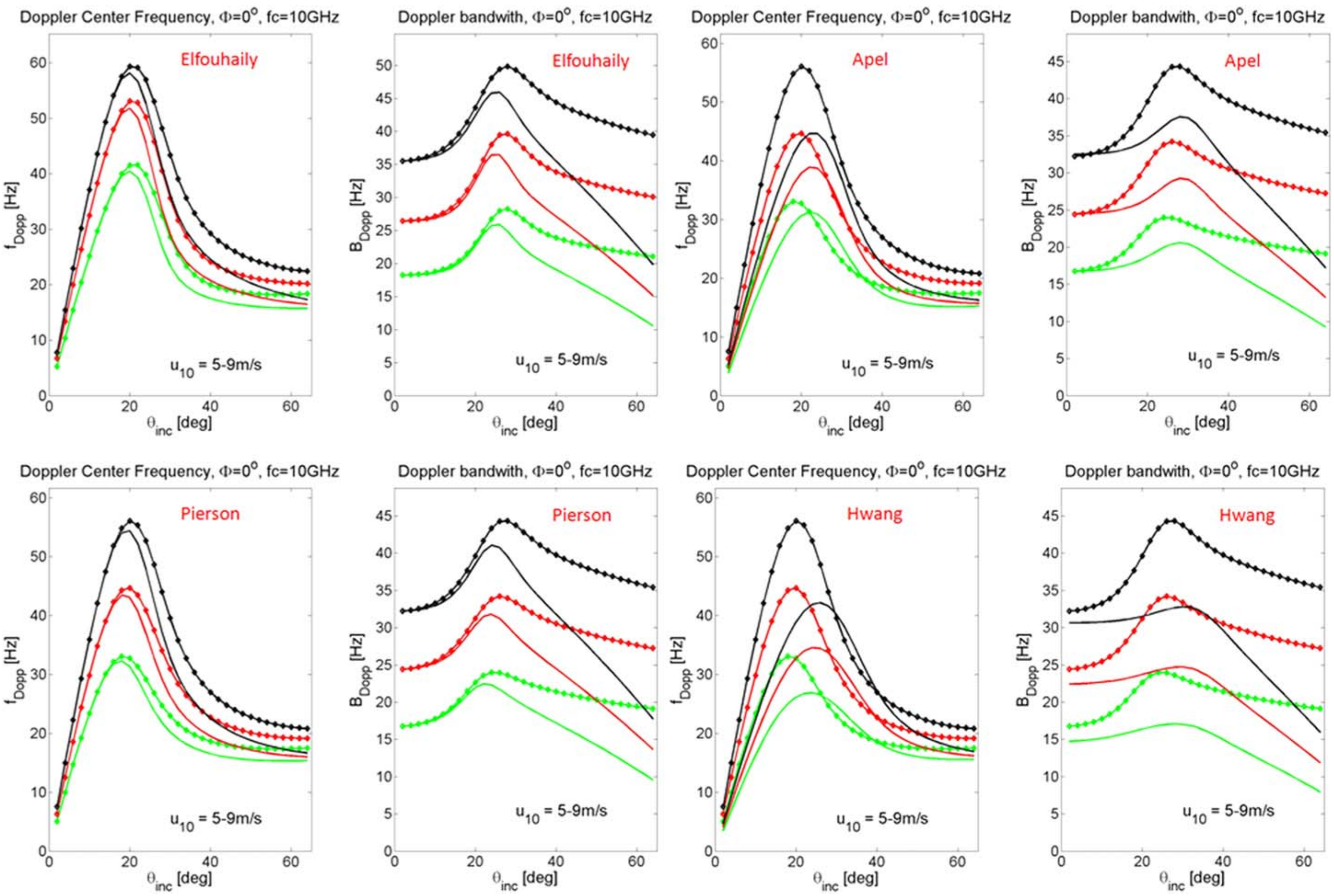

Figure 4. Comparison of KA (solid lines) and KA-CWM (solid lines with diamonds) Doppler shift and Doppler spread, in X-band (10 GHz) for three different wind speeds: 5 m/s (green lines), 7 m/s (read lines), and 9 m/s (black lines), upwind. Four input sea surface wave height spectra are analyzed [*Elfouhaily et al.*, 1997; *Apel*, 1994; *Pierson and Moskowitz*, 1964; *Hwang et al.*, 2011].

when the Elfouhaily unified sea surface spectrum is used. It is also interesting to note that results obtained with the linear sea surface model are much more sensitive to spectral changes than the results obtained with the CWM nonlinear sea surface. This particular behavior explains also why the Doppler signature after CWM transformation is weakly sensitive to the spectral undressing procedure discussed in section 2. In Figure 4, for the linear surface case, the maximum Doppler shift and, also, the maximum Doppler bandwidth occur at different incidence angles depending on the input spectrum. When, instead, the CWM is used, these maximum levels occur approximately at the same incidence angle, which is around 22° for the Doppler shift and around 28° for the Doppler bandwidth. With reference to the results reported by *Nouguier et al*. [2010], a not negligible difference is found on the Doppler bandwidth, at small incidence angles.

This difference is related to the fact that Nouguier *et al*. assumed the waves to travel only toward (or away from) the radar. This means that in equation (3) $S_a(\mathbf{k})$ vanishes in the half-space of wave number pointing to the radar look direction (i.e., $S_a(\mathbf{k})$ is half sided).

In our model, instead, we have made the assumption of a centrosymmetric wave spectrum, where the waves are supposed to move in all directions following the law reported in equation (4).

3.2. The High-Frequency Approximation of SSA2

We have already pointed out that the computation of SSA2 scattering amplitude is very complex as it requires the calculation of fourfold integrals with oscillating functions. To facilitate calculations, *Voronovich and Zavorotny* [2001] performed the following transformation:

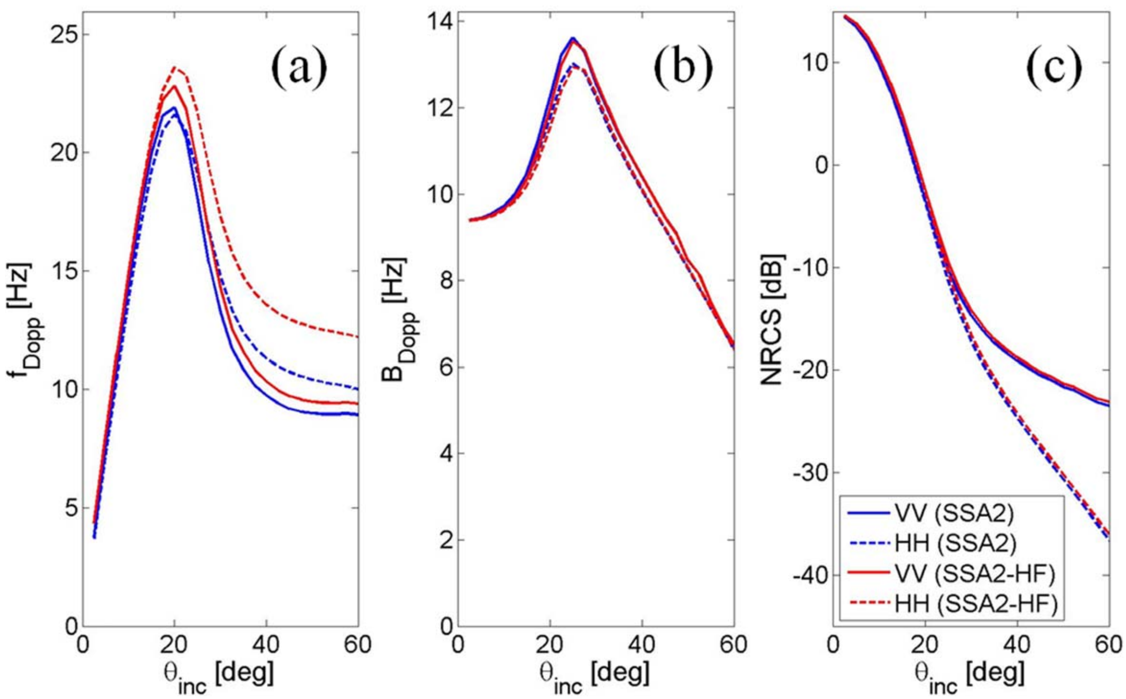

Figure 5. Comparison between SSA2 (linear surface case) and its high-frequency approximation in C-band (5.3 GHz), at 5 m/s upwind. The Elfouhaily spectrum has been used as input for the calculation.

$$B_{\alpha_s\alpha_i}(\mathbf{k}_s,\mathbf{k}_i)-\frac{i}{4}\int M_{\alpha_s\alpha_i}(\mathbf{k}_s,\mathbf{k}_i,\xi)h(\xi,t)e^{j\xi\cdot\mathbf{r}}d\xi \approx$$
$$B_{\alpha_s\alpha_i}(\mathbf{k}_s,\mathbf{k}_i)\cdot \mathrm{Exp}\left[-\frac{i}{4B_{\alpha_s\alpha_i}(\mathbf{k}_s,\mathbf{k}_i)}\int M_{\alpha_s\alpha_i}(\mathbf{k}_s,\mathbf{k}_i,\xi)h(\xi,t)e^{j\xi\cdot\mathbf{r}}d\xi\right]. \tag{40}$$

This simple model is often called High-Frequency Approximation of SSA2, or SSA2-HF. Our simulations confirm the adequacy of this approximation for the computation of the NRCS.

As depicted in Figure 5, in fact, there is no significant difference in NRCS between SSA2 and SSA-HF. We cannot say the same for the Doppler shift, since the high-frequency approximation leads to an overestimation of the Doppler central frequency, particularly for HH-polarization. This is clearly shown in Figure 5a, where the SSA2 model (for a linear surface) and the SSA2-HF model are compared in C-band for wind speed of 5 m/s (upwind). Although, the two models provide about the same Doppler bandwidth (Figure 5b) and the same NRCS (Figure 5c), the estimated Doppler shifts in HH-polarization look very different and this makes the equation (40) questionable when used to accurately estimate the Doppler signature of the sea surface. An additional drawback of this simplified model is its inability to estimate cross-polarized scattering components in the plane of incidence.

4. Simulation Results

4.1. Linear Versus Nonlinear Sea Surface

In this section, we compare the Doppler spectra corresponding to dynamic nonlinear choppy sea surfaces and to linear sea surfaces. The wind speeds used for the comparison are 5, 9, and 13 m/s.

Three incident wave frequencies are analyzed: 5.3 GHz (C-band), 10 GHz (X-band), and 14 GHz (Ku-band). Figure 6 shows Doppler shift, Doppler spread, and normalized radar cross section. Three colors are used to represent the wind speed behavior: the blue lines refer to 5 m/s, red lines to 9 m/s, and finally green lines refer to 13 m/s. Solid lines are used for VV-polarization, dashed lines for HH-polarization, whereas the lines with circles depict the VH-polarization. As anticipated from the theory, we observe a polarization dependency. The predicted wind-induced Doppler shift is larger in HH than in VV-polarization. This result is not surprising, because the radar signal is more sensitive to the smaller waves in VV-polarization than in HH. On the contrary,

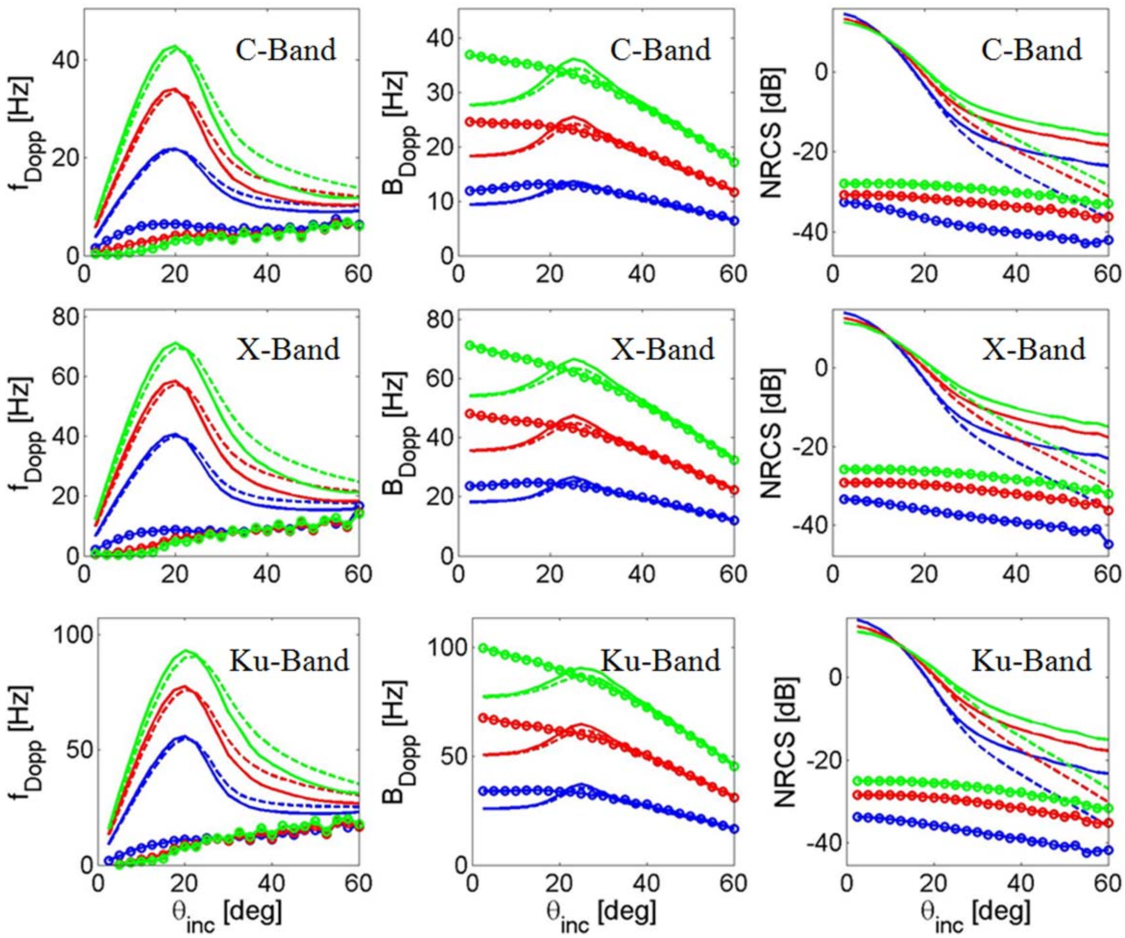

Figure 6. Doppler shift, Doppler bandwidth, and NRCS computed by SSA2-LIN in three different bands: (first row) C-band, (second row) X-band, and (third row) Ku-band. Green lines refer to 13 m/s wind speed (upwind), whereas the red and blue lines refer to 9 and 5 m/s, respectively. Dashed lines are used for HH, solid lines for VV, and circles for VH.

the radar signal is more sensitive to larger propagating waves in HH-polarization than in VV-polarization. Shorter gravity ocean waves are slower, whereas larger propagating waves are faster. As compared to the copolar signals, the cross-polarized backscatter experiences a much lower Doppler shift across the full range of incidence angle investigated, due to its different scattering properties. The Doppler shift of the cross-polarization looks less sensitive to wind speed variations than the copolarization; in fact, the blue, red, and green f_D curves almost overlap above 30° incidence angle. Another important difference is that the central Doppler frequency for the copolar signal shows an evident peak around 22° incidence, whereas this peak is not visible in VH-polarization. For the copolar case, the Doppler width B_D, experiences a peak around 25° incidence, whereas for angles above 25° it decreases almost linearly. For the cross-polar case, instead, B_D, does not show any peak and, at low incidence angle ($\theta_{inc} < 20°$), B_D is expected to be larger than its copolar counterpart. An even more evident difference is observed on the NRCS, which is found weakly sensitive to the incidence angle in VH-polarization (because of the absence of specular contribution in the scattering mechanism) and very sensitive to θ_{inc} in VV and HH-polarization. For a more detailed discussion on the VH-pol. NRCS over the ocean, the reader is referred to *Fois et al.* [2014b], *Van Zadelhoff et al.* [2013], and *Hwang et al.* [2010] where the potential of the cross-polar product to observe and retrieve very strong wind speeds is pointed out.

Figure 7 provides the same information as Figure 6 but for a nonlinear CWM sea surface. At small incidence angles, linear and nonlinear Doppler spectra almost coincide, because the influence of the horizontal velocity component on the Doppler spectrum is small. As the incidence angle increases, nonlinear sea surfaces show larger Doppler central frequency and Doppler spread than the corresponding linear sea surfaces.

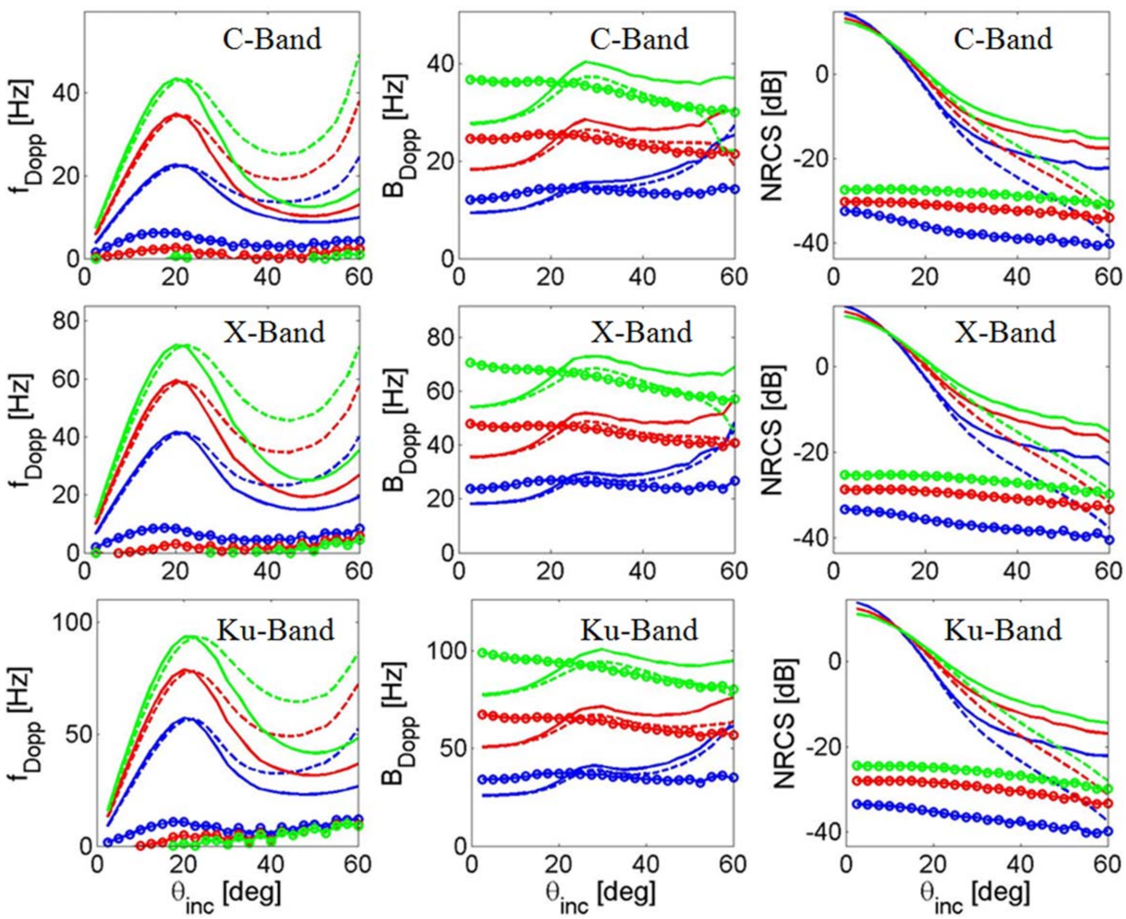

Figure 7. Same as Figure 6 but for SSA2-CWM (see text).

This happens because the Choppy wave model corrects the horizontal component of particle velocities by adding a displacement, related to the surface elevation, to the horizontal position of the particles. These considerations are also supported by the results found in *Toporkov and Brown* [2000], *Li and Xu* [2011], and *Nie et al*. [2012]. In the linear case (see Figure 6), VV and HH Doppler spectra almost overlap at low incidence angles: the relative shift between the two spectra increases with the angle of incidence in the range 20–50° (with the H-pol central Doppler frequency being larger than V-pol one) and eventually decreases at very high incidence angles (i.e., above 50°). For nonlinear surfaces, instead, the relative shift between the two copolar spectra keep growing above 50°, with the horizontal polarization displaying increasingly larger values than the vertical polarization. By comparing Figures 6 and 7, the dependence of the cross-polar Doppler signatures on the wind speed is about the same, with the exception of a small decrease in the cross-polar Doppler shift, as result of the CWM transformation. As already pointed out for the simple KA model, also for SSA2 the Doppler width is found much larger than in the linear case above 30° incidence, where B_D falls off rapidly for linear surfaces. It is worth noting that the Doppler bandwidth in VV-polarization is found larger than the one in HH-polarization, particularly for higher incidences and speeds.

The difference between B_D in VV and B_D in HH is almost negligible at small incidence angles and becomes visible above 30°. Compared to SSA2-CWM, the SSA2-LIN provides slightly different normalized cross section with maximum differences occurring at high incidence angles, up to 1 dB in Ku-band, 1.5 dB in X-band, and about 2 dB in C-band, for the wind speeds investigated.

5. Comparison With Real Measurements and Empirical Geophysical Model Functions

To validate the model, we use the WM (Wave Mode) data collected by the Advanced Synthetic Aperture Radar (ASAR), onboard the Envisat satellite. The C-band (5.35 GHz) instrument was able, during 10 years of

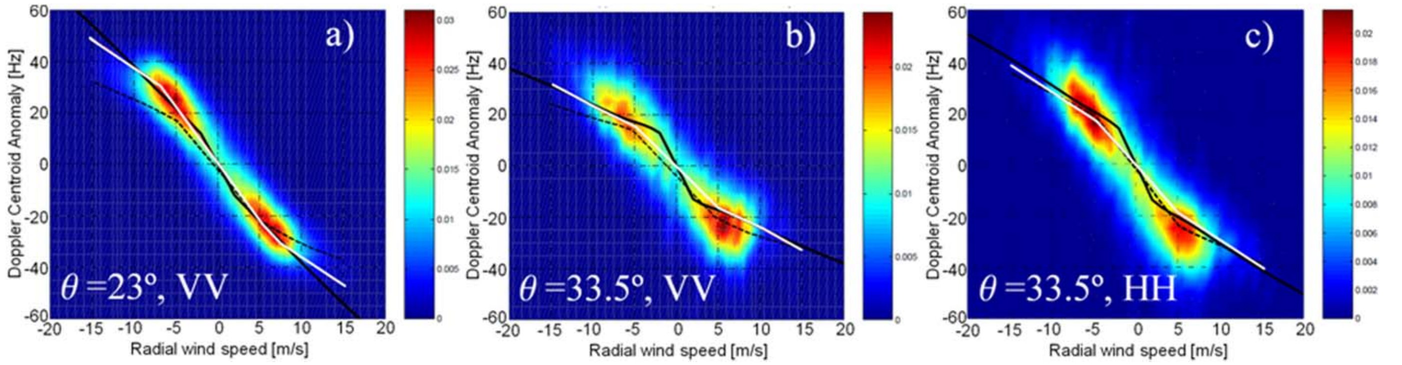

Figure 8. Joint distribution maps of observed Doppler anomaly (in C-band) and line-of-sight winds versus predictions given by our analytical SSA2-CWM (white curves) model for upwind (positive wind speed values) and downwind cases (negative wind speed values). In dashed black, the Doppler shifts provided by the CDOP empirical model and solid black the Doppler shifts as predicted by the high-frequency approximation of the scattering model, proposed by *Mouche et al.* [2008]. (a) VV-polarization and 23° incidence angle; (b) VV-polarization and 33:5° incidence angle; and (c) HH-polarization and 33.5° incidence angle. The colors used in the Doppler maps represent the occurrence of the ASAR measurements.

mission, to obtain measurements of Doppler anomalies versus wind speeds as reported in *Mouche et al*. [2008] and *Chapron et al*. [2005]. Two incidence angles were investigated: 23° in VV-polarization and 33.5° in both VV and HH-polarizations. In both cases, the Doppler shift was evaluated over a 10×10 km^2 area. In *Mouche et al*. [2008], the authors state that with such a resolution cell the effect of sea current on the measurements of central Doppler frequency was negligible. Collocated wind speed and direction measurements were used to find a relationship between the radial wind speed component and the induced Doppler shift.

In Figure 8, we present the results given by our analytical model, based on SSA2-CWM (and Elfouhaily wave height spectrum), considering only wind speeds in up- and downwind direction. The white curves correspond to our model, whereas the dashed black curves refer to the CDOP [*Mouche et al*., 2012] geophysical model function. The solid black line instead refers to the high-frequency approximation of the scattering model, as described in section 4.2 (for a more detailed description of this model, the reader may refer to *Mouche et al*. [2008]). The simulated SSA2-CWM Doppler frequency shifts display a functional relationship versus wind speed in good agreement with the observations, up to a wind speed of ±15 m/s. The consistency of SSA2-CWM with the data at 23° incidence in VV-polarization is particularly remarkable. As shown in Figure 8a, the high-frequency approximation by *Mouche et al*. [2008] reproduces also rather well the ASAR data at 23° in VV-polarization, whereas at 33.5° incidence and low wind speeds it overestimates the Doppler shift for both polarizations. The joint distribution map of Figure 8a looks approximately centrosymmetric: in fact, it shows about the same behavior in upwind and downwind cases, except for the different sign of the Doppler shift. At 33.5° incidence, instead, the joint distribution maps (in VV and HH-polarizations) of observed Doppler anomaly and line-of-sight winds show some asymmetries between upwind and downwind. In particular, the absolute measured Doppler shift in upwind is a few hertz larger than in downwind (see Figures 8b and 8c). The fact that SSA2-CWM was not able to reproduce such asymmetry does not surprise, as the Choppy wave model is a weak nonlinear sea surface model. The measurements collected at 33.5° incidence show that the scatterers in HH-polarization are faster than in VV-polarization: horizontally polarized Doppler spectra are, in fact, shifted toward higher frequencies than the corresponding vertically polarized spectra. This was also observed at X and Ku-band both at sea and in tanks [*Lee et al*., 1995, 1996; *Plant*, 1997; *Plant et al*., 1999] and more recently in L-band [*Forget et al*., 2006]. This phenomenon was interpreted as the manifestation of bound waves or non-Bragg mechanisms. Numerical computations conducted with SSA2-CWM (and reported in Figures 8b and 8c) confirm the role of water waves nonlinearities in the difference between the HH and VV Doppler spectra, by reproducing (both qualitatively and quantitatively) the main features of the observed wind-driven Doppler shift, as a function of incidence angle, wind speed and polarization of the electromagnetic waves. In Figure 9, we have further analyzed the difference between f_D in VV and HH-polarization at four different incidence angles (30, 35, 40, and 45°). Comparison with the CDOP relative Doppler shift between HH and VV-polarization shows a remarkable agreement.

As additional verification, we use the data collected between 10 and 15 December 1991, during phase II of the SAXON-FPN experiment [*Plant and Alpers*, 1994]. Two coherent, continuous wave (CW) microwave systems with pencil beam antennas were operated from the German research platform "NORDSEE." These

Journal of Geophysical Research: Oceans 10.1002/2014JC010589

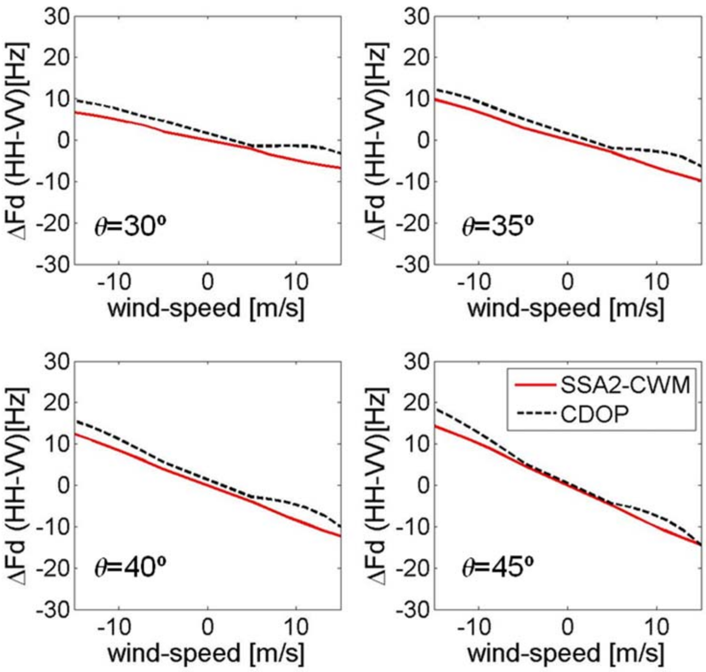

Figure 9. Difference between the VV and HH central Doppler frequency as derived by our analytical SSA2-CWM model (in red) and as provided by the CDOP geophysical model function (in black).

systems operated at Ku and Ka bands, 14 and 35 GHz, respectively. Each system used two antennas, one for transmitting, and one for receiving. Both antennas were dual-polarized, and the two polarizations were separated upon reception by offsetting the transmitted frequencies by 60 MHz. Only like polarizations, HH and VV on transmission and reception, were recorded. One way, half-power antenna beam widths at Ku-band were 6.6° in the *E*-plane and 5.0° in the *H*-plane. The antennas were operated at a height of 26 m above mean low water level

The antenna foot-print on the surface varied from 3 × 5 m at 50° to 5 × 10 m at 80° incidence. The spot sizes were much smaller than the dominant wavelengths which ranged from about 60 to 150 m during the experiment. The presence of sea currents during the measurements is unknown, although one of the instrument deployed during the SAXON-FPN campaign was a current meter. Figure 10 shows an analysis in Ku-band of the measured Doppler shifts and bandwidths at HH and VV-polarization as function of wind speed and direction (for 50 and 60° incidence). The measurements are compared with the analytical SSA2-CWM model. This figure clearly shows the increase in the HH-VV difference with increasing incidence angle when looking upwind and also shows that this difference disappears when the antennas are directed perpendicular to the wind direction.

Furthermore, the data indicate a slight tendency for the offset difference to increase with increasing wind speed for the upwind case. It is worth noting that both VV and HH offsets are negative when the antenna look direction has a downwind component. The modulation of f_D with the wind direction predicted by the model looks overall in good agreement with the measurements taken at different wind speeds. In Figure 10, the squares and the circles refer to VV and HH measurements respectively. Blue, red, and green colors identify the measurements corresponding to wind speeds within the range 0–5, 5–10, and 10–15 m/s, respectively. Overlaid are the simulated results: in particular, solid lines represent VV simulated data and dashed lines HH simulated data. The analysis has been made at three wind speeds: 5 m/s (blue lines), 10 m/s (red lines), and 15 m/s (green lines). From our simulations, the Doppler bandwidth, B_D, is expected to show an almost flat behavior versus the wind direction: this is found consistent with the measurements. As opposed to the real data, the simulations predict a slightly larger bandwidth in V-pol than in H-pol. We have limited our investigation up to 60° incidence, because above this limit the main hypothesis at the basis of the small-slope-approximation theory may be violated, as the tangent of grazing angles of incident/scattered radiation may not sufficiently exceed the rms slope of roughness for most winds.

6. Conclusions and Future Prospective

The Doppler shift measured by a spaceborne active microwave instrument over the ocean can be expressed as the sum of three main terms:

$$f_{D\_Total} = f_{D\_wind} + f_{D\_current} + f_{D\_geometry}. \tag{41}$$

These terms represent the contributions to the central Doppler frequency associated with the wind, e.g., wind drift, (polarization dependent), the ocean current (polarization independent), and the geometry of observation

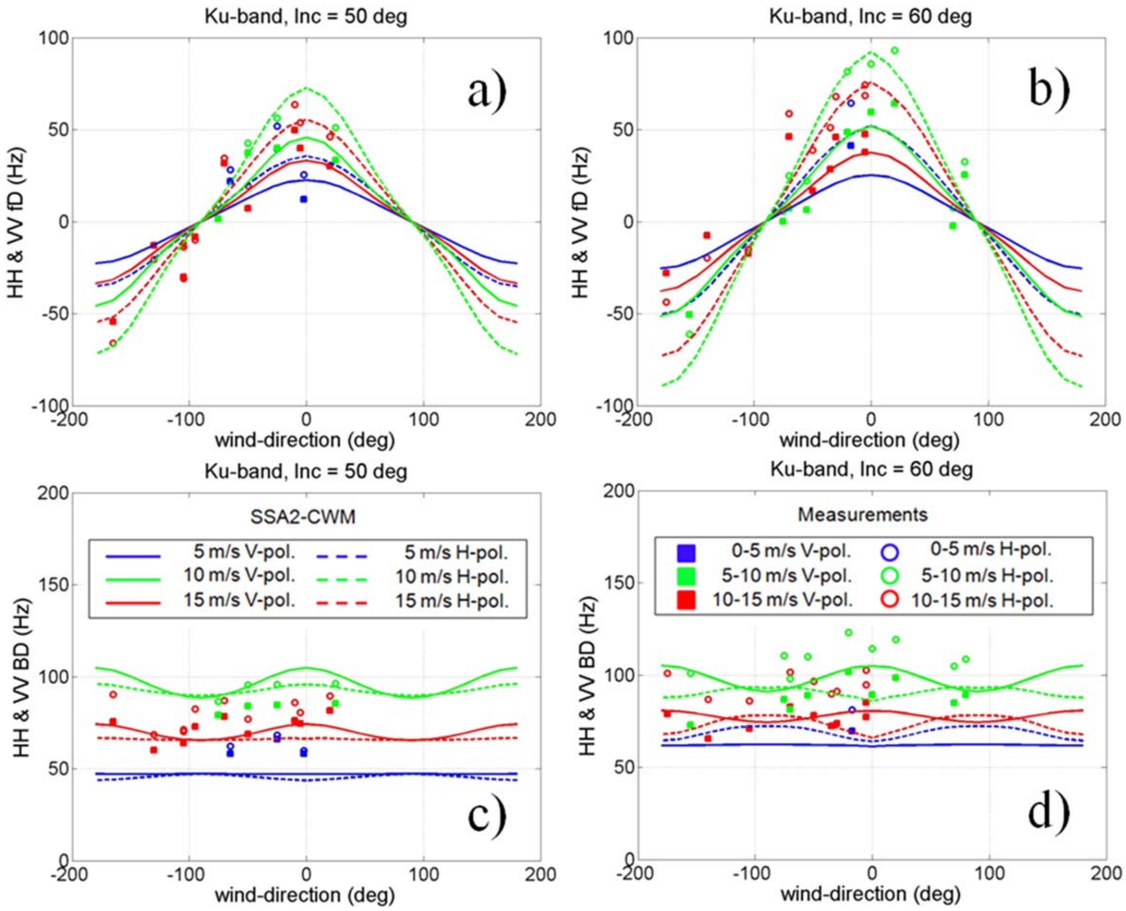

Figure 10. Difference in Ku-band between HH and VV Doppler offsets and spread as function of the angle between the antenna look direction and the wind direction at two incidence angles: (a–c) 50° and (b–d) 60°. Blue, red, and green colors identify the measurements corresponding to wind speeds within the range 0–5, 5–10, and 10–15 m/s, respectively. Overlaid are the simulated results: in particular, solid lines represent VV simulated data and dashed lines HH simulated data. The analysis has been made at three wind speeds: 5 m/s (blue lines), 10 m/s (red lines), and 15 m/s (green lines).

(polarization independent). Nowadays, thanks to the very accurate knowledge of spacecraft attitude and motion, the last term can be easily estimated and removed to get a geophysical Doppler shift or velocity. A last geophysical processing step is then needed to estimate the radial surface current. This final step is definitely the most complex one because it must rely on a Geophysical model function providing the wind driven Doppler shift associated with a specific wind speed and direction. With this picture in mind, the analytical model described in this paper could be a valuable tool to retrieve ocean surface currents. The results reported in the previous sections show that the ocean Doppler spectrum at microwave frequencies can be different for different polarizations. Copolar scattering experiences Doppler frequency shifts higher than the cross-polar scattering. The Doppler shift increases with the wind speed. The rate of this increase depends on the wind directions (as we approach the cross-wind direction, the wind speed sensitivity gets weaker). In principle, we could use the frequency shift between two polarizations (VV-HH, HH-VH, or VV-VH) to identify the wind contribution to the sea surface velocity, thus allowing for the observation of ocean currents.

In this paper, we have presented an analytical model for the full-polarimetric sea surface scattering and Doppler signature based on the small-slope-approximation theory at the second order combined with a weakly nonlinear sea surface representation, named Choppy wave model. This would be the first full-polarimetric physical-based model describing both scattering and Doppler signature of nonlinear sea surfaces. The analytical expression of the model avoids the use of highly demanding Monte-Carlo simulations which are required for more physically based models using exact numerical solution of Maxwell's equations. By using an Intel® Core^{TM} i5–4590 Processor (Quad Core, 3.30GHz Turbo, 8GB DDR3 SDRAM at 1600MHz), no more than 4 h are needed to generate NRCS, Doppler shift and Doppler spread versus incidence and direction angles at five different wind speeds, in three different frequencies bands. All the simulations have been performed considering a 2-D sea surface representation, whereas most of the results in the literature refer to a 1-D sea surface representation. To our knowledge, only few attempts to describe the sea surface scattering and Doppler signature of a 2-D sea surface have been made [*Soriano et al*., 2006; *Li and Xu*, 2011]; but those attempts were always limited, due to computational constraints, to very low wind speeds (<5 m/s) and low frequencies (L-band).

Simplified scattering theories have been derived from the proposed SSA2-CWM model. Simulation results have been compared with real measurements from Envisat-ASAR and from the SAXON-FPN Ku-band campaign, showing remarkable agreement. The results are also consistent with the empirical Geophysical model function CDOP. In future prospective, this model could be used to resolve one of the biggest unknowns in ocean current retrieval: the determination of the wind-driven contribution to the total sea surface Doppler shift. The SSA2-CWM model may also support the definition and the exploitation of new observation principles, based on multipolarimetric Doppler scatterometry, such as the DopSCAT concept [*Fabry et al*., 2013; *Rodriguez et al*., 2014], aiming to provide simultaneous measurements of the ocean vector wind and the ocean vector current on a global scale. The proposed Doppler model is also particularly suited to the interpretation of along-track interferometric synthetic aperture radar data, which include information on surface currents.

Appendix A: Useful Kernals and Covariance Functions

A1. The Bragg Kernels

As clearly discussed in *Voronovich and Zavorotny* [2001], the general expression for the first-order Bragg kernel writes

$$B_{11}(\mathbf{k}_s,\mathbf{k}_i)=2q_{ks}q_{ki}\frac{(\varepsilon_2-1)\quad(q_{ks}^{(2)}q_{ki}^{(2)}\hat{\mathbf{k}}_s\cdot\hat{\mathbf{k}}_i-\varepsilon_2 k_s k_i)}{(\varepsilon_2 q_{ks}^{(1)}+q_{ks}^{(2)})(\varepsilon_2 q_{ki}^{(1)}+q_{ki}^{(2)})},\tag{A1}$$

$$B_{12}(\mathbf{k}_s,\mathbf{k}_i)=2q_{ks}q_{ki}\frac{(\varepsilon_2-1)K_1 q_{ks}^{(2)}(\hat{\mathbf{k}}_s\times\hat{\mathbf{k}}_i)\cdot\hat{\mathbf{z}}}{(\varepsilon_2 q_{ks}^{(1)}+q_{ks}^{(2)})(q_{ki}^{(1)}+q_{ki}^{(2)})},\tag{A2}$$

$$B_{21}(\mathbf{k}_s,\mathbf{k}_i)=2q_{ks}q_{ki}\frac{(\varepsilon_2-1)K_1 q_{ki}^{(2)}(\hat{\mathbf{k}}_s\times\hat{\mathbf{k}}_i)\cdot\hat{\mathbf{z}}}{(q_{ks}^{(1)}+q_{ks}^{(2)})(\varepsilon_2 q_{ki}^{(1)}+q_{ki}^{(2)})},\tag{A3}$$

$$B_{22}(\mathbf{k}_s,\mathbf{k}_i)=-2q_{ks}q_{ki}\frac{(\varepsilon_2-1)K_1^2 q_{ks}^{(2)}(\hat{\mathbf{k}}_s\cdot\hat{\mathbf{k}}_i)}{(q_{ks}^{(1)}+q_{ks}^{(2)})(q_{ki}^{(1)}+q_{ki}^{(2)})}.\tag{A4}$$

The vertical components of the appropriate wave vectors in the first (air) and the second (dielectric) medium are

$$q_{ks}^{(1)}=\sqrt{K_1^2-k_s^2}\quad q_{ks}^{(2)}=\sqrt{\varepsilon_2 K_1^2-k_s^2}\quad \mathrm{Im}\, q_{ks}^{(1,2)}\geq 0,$$

$$q_{ki}^{(1)}=\sqrt{K_1^2-k_i^2}\quad q_{ki}^{(2)}=\sqrt{\varepsilon_2 K_1^2-k_i^2}\quad \mathrm{Im}\, q_{ki}^{(1,2)}\geq 0.$$

The second-order Bragg terms write

$$\begin{aligned}(B_2)_{11}(\mathbf{k}_s,\mathbf{k}_i;\xi)=&\\ \frac{2q_{ks}q_{ki}(\varepsilon_2-1)}{(\varepsilon_2 q_{ks}^{(1)}+q_{ks}^{(2)})(\varepsilon_2 q_{ki}^{(1)}+q_{ki}^{(2)})}&\Bigg[-2\frac{\varepsilon_2-1}{\varepsilon_2 q_{\xi}^{(1)}+q_{\xi}^{(2)}}\\ &(q_{ks}^{(2)}q_{ki}^{(2)}(\hat{\mathbf{k}}_s\cdot\xi)\;(\hat{\mathbf{k}}_i\cdot\xi)+\varepsilon_2 k_s k_i\xi^2)\\ &-(\varepsilon_2 K_1^2(q_{ks}^{(2)}+q_{ki}^{(2)})+2q_{ks}^{(2)}q_{ki}^{(2)}(q_{\xi}^{(1)}-q_{\xi}^{(2)}))(\hat{\mathbf{k}}_s\cdot\hat{\mathbf{k}}_i)\\ &+2\varepsilon_2\frac{q_{\xi}^{(1)}+q_{\xi}^{(2)}}{\varepsilon_2 q_{\xi}^{(1)}+q_{\xi}^{(2)}}(k_i q_{ks}^{(2)}(\hat{\mathbf{k}}_s\cdot\xi)+k_s q_{ki}^{(2)}(\hat{\mathbf{k}}_i\cdot\xi))\Bigg],\end{aligned}\tag{A5}$$

$$(B_2)_{12}(\mathbf{k}_s,\mathbf{k}_i;\xi)= \frac{2q_{ks}q_{ki}(\varepsilon_2-1)K_1}{(\varepsilon_2 q_{ks}^{(1)}+q_{ks}^{(2)})(q_{ki}^{(1)}+q_{ki}^{(2)})}\Bigg[-2\frac{\varepsilon_2-1}{\varepsilon_2 q_\xi^{(1)}+q_\xi^{(2)}} (q_{ks}^{(2)}(\hat{\mathbf{k}}_s\cdot\xi)((\xi\times\hat{\mathbf{k}}_i)\cdot\hat{\mathbf{z}})) -(\varepsilon_2 K_1^2+q_{ks}^{(2)}q_{ki}^{(2)}+2q_{ks}^{(2)}(q_\xi^{(1)}-q_\xi^{(2)}))((\hat{\mathbf{k}}_s\times\hat{\mathbf{k}}_i)\cdot\hat{\mathbf{z}}) +2\varepsilon_2\frac{q_\xi^{(1)}+q_\xi^{(2)}}{\varepsilon_2 q_\xi^{(1)}+q_\xi^{(2)}}k_s((\xi\times\hat{\mathbf{k}}_i)\cdot\hat{\mathbf{z}})\Bigg], \tag{A6}$$

$$(B_2)_{21}(\mathbf{k}_s,\mathbf{k}_i;\xi)= \frac{2q_{ks}q_{ki}(\varepsilon_2-1)K_1}{(q_{ks}^{(1)}+q_{ks}^{(2)})(\varepsilon_2 q_{ki}^{(1)}+q_{ki}^{(2)})}\Bigg[2\frac{\varepsilon_2-1}{\varepsilon_2 q_\xi^{(1)}+q_\xi^{(2)}} (q_{ki}^{(2)}(\hat{\mathbf{k}}_i\cdot\xi)\ ((\xi\times\hat{\mathbf{k}}_s)\cdot\hat{\mathbf{z}})) -(\varepsilon_2 K_1^2+q_{ks}^{(2)}q_{ki}^{(2)}+2q_{ki}^{(2)}(q_\xi^{(1)}-q_\xi^{(2)}))((\hat{\mathbf{k}}_s\times\hat{\mathbf{k}}_i)\cdot\hat{\mathbf{z}}) -2\varepsilon_2\frac{q_\xi^{(1)}+q_\xi^{(2)}}{\varepsilon_2 q_\xi^{(1)}+q_\xi^{(2)}}k_i\Big(\Big((\xi\times\hat{\mathbf{k}}_s)\cdot\hat{\mathbf{z}})\Bigg], \tag{A7}$$

$$(B_2)_{22}(\mathbf{k}_s,\mathbf{k}_i;\xi)= \frac{2q_{ks}q_{ki}(\varepsilon_2-1)K_1^2}{(q_{ks}^{(1)}+q_{ks}^{(2)})(q_{ki}^{(1)}+q_{ki}^{(2)})}\Bigg[-2\frac{\varepsilon_2-1}{\varepsilon_2 q_\xi^{(1)}+q_\xi^{(2)}} ((\hat{\mathbf{k}}_s\cdot\xi)\ \Big(\hat{\mathbf{k}}_i\cdot\xi)-\xi^2\hat{\mathbf{k}}_s\cdot\hat{\mathbf{k}}_i)-(q_{ks}^{(2)}+q_{ki}^{(2)}+2(q_\xi^{(1)}-q_\xi^{(2)}))(\hat{\mathbf{k}}_s\cdot\hat{\mathbf{k}}_i)\Bigg]. \tag{A8}$$

A2. Spatiotemporal Covariance Function Determination for Nonlinear Sea Surfaces

The spatiotemporal covariance function of the backscattered field is the limit of the statistical average for infinity illumination area A

$$Cov(\mathbf{k}_s,\mathbf{k}_i;t)|_{Non-Lin.}= \lim_{A\to\infty}\frac{4\pi\langle|\tilde{\mathbf{S}}_{\alpha_s\alpha_i}^{SSA-2}(\mathbf{k}_s,\mathbf{k}_i,t)-\langle\tilde{\mathbf{S}}_{\alpha_s\alpha_i}^{SSA-2}(\mathbf{k}_s,\mathbf{k}_i,t)\rangle|^2\rangle}{A}= \lim_{A\to\infty}\frac{4\pi(\langle\tilde{\mathbf{S}}_{\alpha_s\alpha_i}^{SSA-2}(\mathbf{k}_s,\mathbf{k}_i,t)\tilde{\mathbf{S}}_{\alpha_s\alpha_i}^{SSA-2*}(\mathbf{k}_s,\mathbf{k}_i,t)\rangle-|\langle\tilde{\mathbf{S}}_{\alpha_s\alpha_i}^{SSA-2}(\mathbf{k}_s,\mathbf{k}_i,t)\rangle|^2)}{A}, \tag{A9}$$

with

$$\langle\tilde{\mathbf{S}}_{\alpha_s\alpha_i}^{SSA-2}(\mathbf{k}_s,\mathbf{k}_i,t)\tilde{\mathbf{S}}_{\alpha_s\alpha_i}^{SSA-2*}(\mathbf{k}_s,\mathbf{k}_i,t)\rangle=\frac{1}{Q_z^2}\int\int\frac{d\mathbf{r}_1}{(2\pi)^2}\frac{d\mathbf{r}_2}{(2\pi)^2}e^{-i\mathbf{Q}_H\cdot(\mathbf{r}_1-\mathbf{r}_2)} \Big\langle e^{iQ_z(h(\mathbf{r}_1,t)-h(\mathbf{r}_2,t))}e^{-i\mathbf{Q}_H\cdot(\mathbf{D}(\mathbf{r}_1,t)-\mathbf{D}(\mathbf{r}_2,t))} \{1+\nabla\cdot\mathbf{D}(\mathbf{r}_1,t)+\nabla\cdot\mathbf{D}(\mathbf{r}_2,t)+(\nabla\cdot\mathbf{D}(\mathbf{r}_1,t))(\nabla\cdot\mathbf{D}(\mathbf{r}_2,t))\} \times\Big\{\ |B_{\alpha_s\alpha_i}(\mathbf{k}_s,\mathbf{k}_i)|^2+ \frac{i}{4}B_{\alpha_s\alpha_i}(\mathbf{k}_s,\mathbf{k}_i)\int M_{\alpha_s\alpha_i}^*(\mathbf{k}_s,\mathbf{k}_i,\xi_2)h^*(\xi_2,t)e^{-i\xi_2\cdot\mathbf{r}_2}d\xi_2 -\frac{i}{4}B_{\alpha_s\alpha_i}^*(\mathbf{k}_s,\mathbf{k}_i)\int M_{\alpha_s\alpha_i}(\mathbf{k}_s,\mathbf{k}_i,\xi_1)h(\xi_1,t)e^{i\xi_1\cdot\mathbf{r}_1}d\xi_1+ \frac{1}{16}\int\int d\xi_1 d\xi_2 M_{\alpha_s\alpha_i}(\mathbf{k}_s,\mathbf{k}_i,\xi_1)M_{\alpha_s\alpha_i}^*(\mathbf{k}_s,\mathbf{k}_i,\xi_2)\cdot h(\xi_1,t)h^*(\xi_2,t)e^{i(\xi_1\cdot\mathbf{r}_1-\xi_2\cdot\mathbf{r}_2)}\Big\}\Big\rangle \tag{A10}$$

and

$$<\tilde{\mathbf{S}}^{SSA-2}_{\alpha_s\alpha_i}(\mathbf{k}_s,\mathbf{k}_i,t)> = $$
$$= \frac{1}{Q_z}\int \frac{d\mathbf{r}}{(2\pi)^2} J(\mathbf{r},t)\exp\left[-i\mathbf{Q}_H\cdot\mathbf{r}\right] < \exp\left[-i\mathbf{Q}_H\cdot D(\mathbf{r},t)+iQ_z h(\mathbf{r},t)\right]$$
$$\times\left[B_{\alpha_s\alpha_i}(\mathbf{k}_s,\mathbf{k}_i)-\frac{i}{4}\int M_{\alpha_s\alpha_i}(\mathbf{k}_s,\mathbf{k}_i,\xi)h(\xi,t)e^{i\xi\cdot\mathbf{r}}d\xi\right] > . \tag{A11}$$

Using standard properties of Gaussian processes [*Papoulis*, 1965], we have

$$Cov(\mathbf{k}_s,\mathbf{k}_i;t)|_{Non-Lin.} = \frac{1}{Q_z^2}\int\frac{d\mathbf{r}}{(2\pi)^2}\tilde{R}_{\alpha_s\alpha_i}(\mathbf{k}_s,\mathbf{k}_i;\mathbf{r},t)\exp\left[-i\mathbf{Q}_H\cdot\mathbf{r}\right], \tag{A12}$$

with

$$\tilde{R}_{\alpha_s\alpha_i}(\mathbf{k}_s,\mathbf{k}_i;\mathbf{r},t) = -|\chi_{\alpha_s\alpha_i}(\mathbf{k}_s,\mathbf{k}_i;t)|^2+\sum_{n=1}^{4}\sum_{m=1}^{4}\Psi^{(m,n)}_{\alpha_s\alpha_i}(\mathbf{k}_s,\mathbf{k}_i;\mathbf{r},t). \tag{A13}$$

The expressions of the different components of $\tilde{R}_{\alpha_s\alpha_i}(\mathbf{k}_s,\mathbf{k}_i;\mathbf{r},t)$ are provided here below.

A2.1. Expression of $\chi_{\alpha_s\alpha_i}$

The term $\chi_{\alpha_s\alpha_i}(\mathbf{k}_s,\mathbf{k}_i;t) = <\tilde{\mathbf{S}}^{SSA-2}_{\alpha_s\alpha_i}(\mathbf{k}_s,\mathbf{k}_i,t)>$ represents the coherent scattered amplitude and it can be expressed as

$$\chi_{\alpha_s\alpha_i}(\mathbf{k}_s,\mathbf{k}_i;t) =$$
$$\mathrm{Exp}\left[\frac{-Q_z^2\sigma_0^2-Q_H^2\sigma^2_{\hat{\mathbf{Q}}_\mathbf{H}}}{2}\right]\left\{(1-iQ_z\sigma_1^2)B_{\alpha_s\alpha_i}(\mathbf{k}_s,\mathbf{k}_i)\ -\frac{i}{4}\int d\xi e^{i\xi\cdot\mathbf{r}}M_{\alpha_s\alpha_i}(\mathbf{k}_s,\mathbf{k}_i,\xi)\cdot\right.$$
$$\left.\left[(1-iQ_z\sigma_1^2)(iQ_zS(\xi,t)-\mathbf{Q}_\mathbf{H}\cdot\hat{\xi}S(\xi,t))-|\xi|S^*(\xi,t)\right]\right\}, \tag{A14}$$

with

$$\begin{cases}\sigma_0^2=C(\mathbf{0},0)=\int d\xi\ \ S(\xi,0)\\ \sigma_1^2=C_1(\mathbf{0},0)=\int d\xi\ \ |\xi|S(\xi,0)\\ \sigma_n^2=C_n(\mathbf{0},0)=\int d\xi\ \ |\xi|^nS(\xi,0)\\ \sigma^2_{\hat{\mathbf{Q}}_\mathbf{H}}=C_{\hat{\mathbf{Q}}_\mathbf{H}}(\mathbf{0},0)=\int d\xi(\hat{\mathbf{Q}}_\mathbf{H}\cdot\hat{\xi})^2\ \ S(\xi,0)\end{cases}. \tag{A15}$$

A2.2. Expression of $\Psi^{(1,1)}_{\alpha_s\alpha_i}$

The term $\Psi^{(1,1)}_{\alpha_s\alpha_i}$ in equation (A9) is simply given by

$$\Psi^{(1,1)}_{\alpha_s\alpha_i}(\mathbf{k}_s,\mathbf{k}_i;\mathbf{r},t)=|B_{\alpha_s\alpha_i}(\mathbf{k}_s,\mathbf{k}_i)|^2 Exp\left[\frac{-Q_z^2S_0(\mathbf{r},t)-Q_H^2S_{\hat{\mathbf{Q}}_\mathbf{H}}(\mathbf{r},t)}{2}\right]=|B_{\alpha_s\alpha_i}(\mathbf{k}_s,\mathbf{k}_i)|^2E(\mathbf{r},t), \tag{A16}$$

with

$$\begin{cases}S_0(\mathbf{r},t)=2[\sigma_0^2-C(\mathbf{r},t)]\\ S_{\hat{\mathbf{Q}}_\mathbf{H}}(\mathbf{r},t)=2[\sigma^2_{\hat{\mathbf{Q}}_\mathbf{H}}-C_{\hat{\mathbf{Q}}_\mathbf{H}}(\mathbf{r},t)]\\ C_{\hat{\mathbf{Q}}_\mathbf{H}}(\mathbf{r},t)=\int d\xi(\hat{\mathbf{Q}}_\mathbf{H}\cdot\hat{\xi})^2\ \ S(\xi,t)e^{i\mathbf{r}\cdot\xi}\end{cases} \tag{A17}$$

and

$$E(\mathbf{r},t)=\mathrm{Exp}\left[\frac{-Q_z^2S_0(\mathbf{r},t)-Q_H^2S_{\hat{\mathbf{Q}}_\mathbf{H}}(\mathbf{r},t)}{2}\right]. \tag{A18}$$

A2.3. Expression of $\Psi^{(1,2)}_{\alpha_s\alpha_i}$

The term $\Psi^{(1,2)}_{\alpha_s\alpha_i}$ in equation (A13) has the following form:

$$\Psi^{(1,2)}_{\alpha_s\alpha_i}(\mathbf{k}_s,\mathbf{k}_i;\mathbf{r},t)=\frac{i}{4}B_{\alpha_s\alpha_i}(\mathbf{k}_s,\mathbf{k}_i)\mathrm{Exp}\left[\frac{-Q_z^2S_0(\mathbf{r},t)-Q_H^2S_{\hat{\mathbf{Q}}_\mathbf{H}}(\mathbf{r},t)}{2}\right]\times \int d\xi M^*_{\alpha_s\alpha_i}(\mathbf{k}_s,\mathbf{k}_i;\xi)S^*(\xi,t)\{(e^{i\mathbf{r}\cdot\xi}-1)[iQ_Z-\mathbf{Q_H}\cdot\hat{\xi}]\}, \tag{A19}$$

or equivalently

$$\begin{aligned}\Psi^{(1,2)}_{\alpha_s\alpha_i}(\mathbf{k}_s,\mathbf{k}_i;\mathbf{r},t)=&\ \frac{i}{4}B_{\alpha_s\alpha_i}(\mathbf{k}_s,\mathbf{k}_i)E(\mathbf{r},t)\times\int d\xi M^*_{\alpha_s\alpha_i}(\mathbf{k}_s,\mathbf{k}_i;\xi)Z_2(\xi,t)=\\ =&\ \frac{i}{4}B_{\alpha_s\alpha_i}(\mathbf{k}_s,\mathbf{k}_i)E(\mathbf{r},t)\cdot mzd(\mathbf{k}_s,\mathbf{k}_i;\mathbf{r},t),\end{aligned} \tag{A20}$$

being

$$\begin{cases} Z_2(\xi,t)=S^*(\xi,t)\{(e^{i\mathbf{r}\cdot\xi}-1)[iQ_Z-\mathbf{Q_H}\cdot\hat{\xi}]\} \\ mzd(\mathbf{k}_s,\mathbf{k}_i;\mathbf{r},t)=\int d\xi M^*_{\alpha_s\alpha_i}(\mathbf{k}_s,\mathbf{k}_i;\xi)Z_2(\xi,t)\end{cases}. \tag{A21}$$

In order to simplify the notation, the dependence of mzd on α_s,α_i will be intentionally omitted.

A2.4. Expression of $\Psi^{(1,3)}_{\alpha_s\alpha_i}$

Similarly to $\Psi^{(1,2)}_{\alpha_s\alpha_i}$, the term $\Psi^{(1,3)}_{\alpha_s\alpha_i}$ can be written as

$$\Psi^{(1,3)}_{\alpha_s\alpha_i}(\mathbf{k}_s,\mathbf{k}_i;\mathbf{r},t)= -\frac{i}{4}B^*_{\alpha_s\alpha_i}(\mathbf{k}_s,\mathbf{k}_i)\mathrm{Exp}\left[\frac{-Q_z^2S_0(\mathbf{r},t)-Q_H^2S_{\hat{\mathbf{Q}}_\mathbf{H}}(\mathbf{r},t)}{2}\right]\times \int d\xi M_{\alpha_s\alpha_i}(\mathbf{k}_s,\mathbf{k}_i;\xi)S(\xi,t)\{(1-e^{i\mathbf{r}\cdot\xi})[iQ_Z+\mathbf{Q_H}\cdot\hat{\xi}]\}. \tag{A22}$$

We also define

$$\begin{cases} Z_1(\xi,t)=S(\xi,t)\{(1-e^{i\mathbf{r}\cdot\xi})[iQ_Z+\mathbf{Q_H}\cdot\hat{\xi}]\} \\ mzu(\mathbf{k}_s,\mathbf{k}_i;\mathbf{r},t)=\int d\xi M_{\alpha_s\alpha_i}(\mathbf{k}_s,\mathbf{k}_i;\xi)Z_1(\xi,t)\end{cases}, \tag{A23}$$

thus

$$\Psi^{(1,3)}_{\alpha_s\alpha_i}(\mathbf{k}_s,\mathbf{k}_i;\mathbf{r},t)=-\frac{i}{4}B^*_{\alpha_s\alpha_i}(\mathbf{k}_s,\mathbf{k}_i)E(\mathbf{r},t)\times mzu(\mathbf{k}_s,\mathbf{k}_i;\mathbf{r},t). \tag{A24}$$

In order to simplify the notation, the dependence of mzu on α_s,α_i will be intentionally omitted.

A2.5. Expression of $\Psi^{(1,4)}_{\alpha_s\alpha_i}$

The term $\Psi^{(1,4)}_{\alpha_s\alpha_i}$ is the result of two double integrals, one over the wave number vector ξ_1 and the other over the wave number vector ξ_2

$$\begin{aligned}\Psi^{(1,4)}_{\alpha_s\alpha_i}(\mathbf{k}_s,\mathbf{k}_i;\mathbf{r},t)=\frac{1}{16}\mathrm{Exp}\left[\frac{-Q_z^2S_0(\mathbf{r},t)-Q_H^2S_{\hat{\mathbf{Q}}_\mathbf{H}}(\mathbf{r},t)}{2}\right]\times\int\int d\xi_1 d\xi_2 M_{\alpha_s\alpha_i}(\mathbf{k}_s,\mathbf{k}_i;\xi_1)\cdot\\ M^*_{\alpha_s\alpha_i}(\mathbf{k}_s,\mathbf{k}_i;\xi_2)\{S(\xi_1,t)e^{i\mathbf{r}\cdot\xi_2}\delta(\xi_1-\xi_2)+\left[S(\xi_1,t)(1-e^{i\mathbf{r}\cdot\xi_1})[iQ_Z+\mathbf{Q_H}\cdot\hat{\xi}_1]\right]\times\\ \left[S^*(\xi_2,t)(e^{i\mathbf{r}\cdot\xi_2}-1)[iQ_Z-\mathbf{Q_H}\cdot\hat{\xi}_2]\right]\},\end{aligned} \tag{A25}$$

and it can be also expressed as

$$\Psi^{(1,4)}_{\alpha_s\alpha_i}(\mathbf{k}_s,\mathbf{k}_i;\mathbf{r},t)=\frac{1}{16}\mathrm{Exp}\left[\frac{-Q_Z^2S_0(\mathbf{r},t)-Q_H^2S_{\hat{\mathbf{Q}}_\mathbf{H}}(\mathbf{r},t)}{2}\right]\times\left\{\int d\xi|M_{\alpha_s\alpha_i}(\mathbf{k}_s,\mathbf{k}_i;\xi)|^2S(\xi,t)e^{i\mathbf{r}\cdot\xi}+\right.$$
$$\int d\xi_1M_{\alpha_s\alpha_i}(\mathbf{k}_s,\mathbf{k}_i;\xi_1)S(\xi_1,t)\times\left[(1-e^{i\mathbf{r}\cdot\xi_1})[iQ_Z+\mathbf{Q_H}\cdot\hat{\xi}_1]\right]\times\int d\xi_2M^*_{\alpha_s\alpha_i}(\mathbf{k}_s,\mathbf{k}_i;\xi_2)S^*(\xi_2,t)\times \tag{A26}$$
$$\left.\left[(e^{i\mathbf{r}\cdot\xi_2}-1)[iQ_Z-\mathbf{Q_H}\cdot\hat{\xi}_2]\right]\right\}$$

and by using a more compact notation

$$\Psi^{(1,4)}_{\alpha_s\alpha_i}(\mathbf{k}_s,\mathbf{k}_i;\mathbf{r},t)=\frac{1}{16}E(\mathbf{r},t)\times\{mzq(\mathbf{k}_s,\mathbf{k}_i;\mathbf{r},t)+\ mzu(\mathbf{k}_s,\mathbf{k}_i;\mathbf{r},t)\cdot mzd(\mathbf{k}_s,\mathbf{k}_i;\mathbf{r},t)\}, \tag{A27}$$

where

$$mzq(\mathbf{k}_s,\mathbf{k}_i;\mathbf{r},t)=\int d\xi|M_{\alpha_s\alpha_i}(\mathbf{k}_s,\mathbf{k}_i;\xi)|^2S(\xi,t)e^{i\mathbf{r}\cdot\xi}. \tag{A28}$$

The dependence of mzq on α_s, α_i has been intentionally omitted in order to simplify the notation.

A2.6. Expression of $\Psi^{(2,1)}_{\alpha_s\alpha_i}$

The term $\Psi^{(2,1)}_{\alpha_s\alpha_i}$ can be calculated as a product of three terms

$$\Psi^{(2,1)}_{\alpha_s\alpha_i}(\mathbf{k}_s,\mathbf{k}_i;\mathbf{r},t)=|B_{\alpha_s\alpha_i}(\mathbf{k}_s,\mathbf{k}_i)|^2\mathrm{Exp}\left[\frac{-Q_Z^2S_0(\mathbf{r},t)-Q_H^2S_{\hat{\mathbf{Q}}_\mathbf{H}}(\mathbf{r},t)}{2}\right]\times\left[-\frac{Q_ZS_1(\mathbf{r},t)}{2}+\mathbf{Q_H}\cdot\nabla C(\mathbf{r},t)\right], \tag{A29}$$

or, equivalently

$$\Psi^{(2,1)}_{\alpha_s\alpha_i}(\mathbf{k}_s,\mathbf{k}_i;\mathbf{r},t)=|B_{\alpha_s\alpha_i}(\mathbf{k}_s,\mathbf{k}_i)|^2E(\mathbf{r},t)\times\ i\ R_1(\mathbf{k}_s,\mathbf{k}_i;\mathbf{r},t),$$

where

$$\begin{cases} S_1(\mathbf{r},t)=2[\sigma_1^2-C_1(\mathbf{r},t)]=2\int d\xi|\xi|[S(\xi,0)-S(\xi,t)e^{i\xi\cdot\mathbf{r}}] \\ \hat{\mathbf{Q}}_\mathbf{H}\cdot\nabla C(\mathbf{r},t)=i\int d\xi(\hat{\mathbf{Q}}_\mathbf{H}\cdot\xi)\ \ S(\xi,t)e^{i\mathbf{r}\cdot\xi} \end{cases} \tag{A30}$$

and

$$R_1(\mathbf{k}_s,\mathbf{k}_i;\mathbf{r},t)=-\frac{Q_ZS_1(\mathbf{r},t)}{2}+\mathbf{Q_H}\cdot\nabla C(\mathbf{r},t).$$

A2.7. Expression of $\Psi^{(2,2)}_{\alpha_s\alpha_i}$

The term $\Psi^{(2,2)}_{\alpha_s\alpha_i}$ in equation (A13) has the following form:

$$\Psi^{(2,2)}_{\alpha_s\alpha_i}(\mathbf{k}_s,\mathbf{k}_i;\mathbf{r},t)=\frac{i}{4}B_{\alpha_s\alpha_i}(\mathbf{k}_s,\mathbf{k}_i)E(\mathbf{r},t)\times\{msd_\mathbf{r}(\mathbf{k}_s,\mathbf{k}_i;\mathbf{r},t)+i\cdot mzd(\mathbf{k}_s,\mathbf{k}_i;\mathbf{r},t)\cdot R_1(\mathbf{r},t)\}, \tag{A31}$$

where

$$\begin{cases} msd_\mathbf{r}(\mathbf{k}_s,\mathbf{k}_i;\mathbf{r},t)=\int d\xi M^*_{\alpha_s\alpha_i}(\mathbf{k}_s,\mathbf{k}_i;\xi)\chi_2(\xi,t)e^{i\mathbf{r}\cdot\xi} \\ \chi_2(\xi,t)=|\xi|S(\xi,t) \end{cases}, \tag{A32}$$

omitting the dependence of msd_r on the polarization.

A2.8. Expression of $\Psi^{(2,3)}_{\alpha_s\alpha_i}$

As for $\Psi^{(2,2)}_{\alpha_s\alpha_i}$, the term $\Psi^{(2,3)}_{\alpha_s\alpha_i}$ can be computed as

$$\Psi^{(2,3)}_{\alpha_s\alpha_i}(\mathbf{k}_s,\mathbf{k}_i;\mathbf{r},t)=-\frac{i}{4}B^*_{\alpha_s\alpha_i}(\mathbf{k}_s,\mathbf{k}_i)E(\mathbf{r},t)\times\{msu_\mathbf{0}(\mathbf{k}_s,\mathbf{k}_i;0,t)+i\cdot mzu(\mathbf{k}_s,\mathbf{k}_i;\mathbf{r},t)\cdot R_1(\mathbf{k}_s,\mathbf{k}_i;\mathbf{r},t)\}, \tag{A33}$$

where

$$\begin{cases} msu_{\mathbf{0}}(\mathbf{k}_s,\mathbf{k}_i;0,t)=\int d\xi M(\mathbf{k}_s,\mathbf{k}_i;\xi)\chi_1(\xi,t) \\ \chi_1(\xi,t)=|\xi|S^*(\xi,t) \end{cases}. \tag{A34}$$

For the sake of notation simplicity, the dependence of msu_0 on the polarization has been intentionally omitted.

A2.9. Expression of $\Psi^{(2,4)}_{\alpha_s\alpha_i}$

The compact form of $\Psi^{(2,4)}_{\alpha_s\alpha_i}$ is

$$\Psi^{(2,4)}_{\alpha_s\alpha_i}(\mathbf{k}_s,\mathbf{k}_i;\mathbf{r},t)=\frac{1}{16}E(\mathbf{r},t)\times\{msu_{\mathbf{0}}\cdot mzd+i\cdot mzq\cdot R_1+mzu\cdot msd_{\mathbf{r}}+i\cdot mzu\cdot mzd\cdot R_1\}, \tag{A35}$$

where the dependence of the different functions on $\mathbf{k}_s,\mathbf{k}_i;\mathbf{r},t$ has been intentionally omitted to simplify the notation.

A2.10. Expression of $\Psi^{(3,1)}_{\alpha_s\alpha_i}$

This term can be expressed as

$$\begin{aligned}\Psi^{(3,1)}_{\alpha_s\alpha_i}(\mathbf{k}_s,\mathbf{k}_i;\mathbf{r},t)&=|B_{\alpha_s\alpha_i}(\mathbf{k}_s,\mathbf{k}_i)|^2\mathrm{Exp}\left[\frac{-Q_z^2S_0(\mathbf{r},t)-Q_H^2S_{\hat{\mathbf{Q}}_\mathbf{H}}(\mathbf{r},t)}{2}\right]\times\left[\frac{Q_zS_1(\mathbf{r},t)}{2}-\mathbf{Q_H}\cdot\nabla C(\mathbf{r},t)\right]\\&=|B_{\alpha_s\alpha_i}(\mathbf{k}_s,\mathbf{k}_i)|^2E(\mathbf{r},t)\times i\ R_2(\mathbf{k}_s,\mathbf{k}_i;\mathbf{r},t),\end{aligned} \tag{A36}$$

with

$$R_2(\mathbf{k}_s,\mathbf{k}_i;\mathbf{r},t)=\frac{Q_zS_1(\mathbf{r},t)}{2}+\mathbf{Q_H}\cdot\nabla C(\mathbf{r},t).$$

A2.11. Expression of $\Psi^{(3,2)}_{\alpha_s\alpha_i}$

The expression of $\Psi^{(3,2)}_{\alpha_s\alpha_i}$ is similar to the one of $\Psi^{(2,2)}_{\alpha_s\alpha_i}$

$$\Psi^{(3,2)}_{\alpha_s\alpha_i}(\mathbf{k}_s,\mathbf{k}_i;\mathbf{r},t)=\frac{i}{4}B_{\alpha_s\alpha_i}(\mathbf{k}_s,\mathbf{k}_i)E(\mathbf{r},t)\times\{msd_{\mathbf{0}}+i\cdot mzd\cdot R_2\}, \tag{A37}$$

with

$$msd_{\mathbf{0}}(\mathbf{k}_s,\mathbf{k}_i;0,t)=\int d\xi M^*_{\alpha_s\alpha_i}(\mathbf{k}_s,\mathbf{k}_i;\xi)\chi_2(\xi,t). \tag{A38}$$

For simplicity, we have omitted from the notation the dependence of msd_0 on the polarization.

A2.12. Expression of $\Psi^{(3,3)}_{\alpha_s\alpha_i}$

As for $\Psi^{(3,2)}_{\alpha_s\alpha_i}$, the term $\Psi^{(3,3)}_{\alpha_s\alpha_i}$ can be expressed as

$$\Psi^{(3,3)}_{\alpha_s\alpha_i}(\mathbf{k}_s,\mathbf{k}_i;\mathbf{r},t)=-\frac{i}{4}B^*_{\alpha_s\alpha_i}(\mathbf{k}_s,\mathbf{k}_i)E(\mathbf{r},t)\times\{msu_{\mathbf{r}}+i\cdot mzu\cdot R_2\}, \tag{A39}$$

with

$$msu_{\mathbf{r}}(\mathbf{k}_s,\mathbf{k}_i;\mathbf{r},t)=\int d\xi M_{\alpha_s\alpha_i}(\mathbf{k}_s,\mathbf{k}_i;\xi)\chi_1(\xi,t)e^{i\mathbf{r}\cdot\xi}. \tag{A40}$$

A2.13. Expression of $\Psi^{(3,4)}_{\alpha_s\alpha_i}$

The term $\Psi^{(3,4)}_{\alpha_s\alpha_i}$ can be expressed as sum of four main elements

$$\Psi^{(3,4)}_{\alpha_s\alpha_i}(\mathbf{k}_s,\mathbf{k}_i;\mathbf{r},t)=\frac{1}{16}E(\mathbf{r},t)\times\{msu_{\mathbf{r}}\cdot mzd+i\cdot mzq\cdot R_2+mzu\cdot msd_{\mathbf{0}}+i\cdot mzu\cdot mzd\cdot R_2\}. \tag{A41}$$

A2.14. Expression of $\Psi^{(4,1)}_{\alpha_s\alpha_i}$

After simple manipulations, this term can be written as

$$\Psi^{(4,1)}_{\alpha_s\alpha_i}(\mathbf{k}_s,\mathbf{k}_i;\mathbf{r},t)=|B_{\alpha_s\alpha_i}(\mathbf{k}_s,\mathbf{k}_i)|^2E(\mathbf{r},t)\times\{-\Delta C(\mathbf{r},t)-\ R_1\ \ \cdot R_2\}, \tag{A42}$$

where $\Delta C(\mathbf{r},t)$ is the Laplacian operator, that is,

$$\Delta C(\mathbf{r},t)=\nabla\cdot\nabla C(\mathbf{r},t)=-\int d\xi|\xi|^2 S(\xi,t)e^{i\mathbf{r}\cdot\xi}. \tag{A43}$$

A2.15. Expression of $\Psi^{(4,2)}_{\alpha_s\alpha_i}$

$$\Psi^{(4,2)}_{\alpha_s\alpha_i}(\mathbf{k}_s,\mathbf{k}_i;\mathbf{r},t)=\frac{i}{4}B_{\alpha_s\alpha_i}(\mathbf{k}_s,\mathbf{k}_i)E(\mathbf{r},t)\times\{i\cdot msd_{\mathbf{0}}\cdot R_1+i\cdot msd_{\mathbf{r}}\cdot R_2+mzd\cdot[-\Delta C-\ R_1R_2]\}. \tag{A44}$$

A2.16. Expression of $\Psi^{(4,3)}_{\alpha_s\alpha_i}$

$$\Psi^{(4,3)}_{\alpha_s\alpha_i}(\mathbf{k}_s,\mathbf{k}_i;\mathbf{r},t)=-\frac{i}{4}B^*_{\alpha_s\alpha_i}(\mathbf{k}_s,\mathbf{k}_i)E(\mathbf{r},t)\times\{i\cdot msu_{\mathbf{r}}\cdot R_1+i\cdot msu_{\mathbf{0}}\cdot R_2+mzu\cdot[-\Delta C-\ R_1R_2]\}. \tag{A45}$$

A2.17. Expression of $\Psi^{(4,4)}_{\alpha_s\alpha_i}$

The last term of the summation in equation (A13) is

$$\begin{aligned}\Psi^{(4,4)}_{\alpha_s\alpha_i}(\mathbf{k}_s,\mathbf{k}_i;\mathbf{r},t)=\frac{1}{16}E(\mathbf{r},t)\times\{&msu_{\mathbf{0}}\cdot msd_{\mathbf{0}}+msu_{\mathbf{r}}\cdot msd_{\mathbf{r}}+i\cdot msu_{\mathbf{r}}\cdot mzd\cdot R_1\\ &+i\cdot msu_{\mathbf{0}}\cdot mzd\cdot R_2+i\cdot msd_{\mathbf{r}}\cdot mzu\cdot R_2+i\cdot msd_{\mathbf{0}}\cdot mzu\cdot R_1+mzq\cdot[-\Delta C-\ R_1R_2]+\\ &+mzu\cdot mzd\cdot[-\Delta C-\ R_1R_2]\}.\end{aligned} \tag{A46}$$

A3. Some Important Analytical Expressions

In the case of sea surface spectra with two azimuthal harmonics, the correlation functions and related Kirchhoff integrals can be efficiently computed with the help of the Bessel functions. The two-dimensional sea spectrum can be expressed as

$$S(\xi,t)=S_a(\xi)\exp(-i\omega_\xi t)+S_a(-\xi)\exp(i\omega_\xi t), \tag{A47}$$

where

$$\begin{cases} S_a(\xi)=S(\xi)\cos^2\left(\dfrac{\varphi-\varphi_w}{2}\right)=S(\xi)\cos^2\left(\dfrac{\Theta}{2}\right)\\ S_a(-\xi)=S(\xi)\sin^2\left(\dfrac{\varphi-\varphi_w}{2}\right)=S(\xi)\sin^2\left(\dfrac{\Theta}{2}\right)\end{cases}, \tag{A48}$$

being Θ the angle with respect to the wind direction. The centrosymmetric spectrum $S(\xi)$ is equal to

$$S(\xi)=M(\xi)(1+\Delta(\xi)\cos(2\Theta)). \tag{A49}$$

The function $M(\xi)$ represents the isotropic part of the spectrum modulated by $1+\Delta(\xi)\cos(2\Theta)$, corresponding to the angular function. With the previous assumptions, the correlation function can be written as

$$\begin{aligned}C(\mathbf{r},t)=\int d\xi\ S(\xi,t)\exp(i\ \xi\cdot\mathbf{r})=\int_0^\infty\int_0^{2\pi}d\xi d\Theta\xi[S_a(\xi)\exp(-i\omega_\xi t)+S_a(-\xi)\exp(i\omega_\xi t)]\times\exp[ir\xi\cos(\Theta-\phi_r)]=\\ \int_0^\infty d\xi\left[\sum_{n=-\infty}^{\infty}\frac{(i)^n e^{in\phi_r}}{2\pi}J_n(r\xi)\left\{\exp(-i\omega_\xi t)\times\int_0^{2\pi}d\Theta\xi\ M(\xi)(1+\Delta(\xi)\cos(2\Theta))\cos^2\left(\frac{\Theta}{2}\right)e^{in\Theta}+\right.\right.\\ \left.\left.\exp(i\omega_\xi t)\int_0^{2\pi}d\Theta\xi\ M(\xi)(1+\Delta(\xi)\cos(2\Theta))\sin^2\left(\frac{\Theta}{2}\right)e^{in\Theta}\right\}\right],\end{aligned} \tag{A50}$$

where $J_n(r\xi)$ is the Bessel function of order n. After some straightforward calculation, we obtain

$$C(\mathbf{r},t)=\int_0^\infty d\xi\xi\left\{\cos(\omega_\xi t)M(\xi)\times[J_0(r\xi)-J_2(r\xi)\Delta(\xi)\cos(2\phi_r)]+\frac{1}{2}\sin(\omega_\xi t)M(\xi)\times\right.$$
$$\left.[(2+\Delta(\xi))J_1(r\xi)\cos(\phi_r)-\Delta(\xi)J_3(r\xi)\cos(3\phi_r)]\right\}. \tag{A51}$$

Similarly for $\Delta C(\mathbf{r},t)$ and $C_1(\mathbf{r},t)$ we get

$$\Delta C(\mathbf{r},t)=-\int_0^\infty d\xi\xi\left\{\cos(\omega_\xi t)\xi^2M(\xi)\times[J_0(r\xi)-J_2(r\xi)\Delta(\xi)\cos(2\phi_r)]+\frac{1}{2}\sin(\omega_\xi t)\xi^2M(\xi)\times\right.$$
$$\left.[(2+\Delta(\xi))J_1(r\xi)\cos(\phi_r)-\Delta(\xi)J_3(r\xi)\cos(3\phi_r)]\right\} \tag{A52}$$

and

$$C_1(\mathbf{r},t)=\int_0^\infty d\xi\xi\left\{\cos(\omega_\xi t)\xi M(\xi)\times[J_0(r\xi)-J_2(r\xi)\Delta(\xi)\cos(2\phi_r)]+\frac{1}{2}\sin(\omega_\xi t)\xi M(\xi)\times\right.$$
$$\left.[(2+\Delta(\xi))J_1(r\xi)\cos(\phi_r)-\Delta(\xi)J_3(r\xi)\cos(3\phi_r)]\right\}. \tag{A53}$$

With some algebra we obtain also

$$\hat{\mathbf{Q}}_{\mathbf{H}}\cdot\nabla C(\mathbf{r},t)=\int_0^\infty d\xi\xi\cos(\omega_\xi t)\{-J_1(r\xi)\xi M(\xi)\cos(\phi_r-\phi_{\hat{\mathbf{Q}}_{\mathbf{H}}})$$
$$-\frac{1}{2}[(J_1(r\xi)-J_3(r\xi))\xi M(\xi)\Delta(\xi)\cos(\phi_r-\phi_{\hat{\mathbf{Q}}_{\mathbf{H}}})\cos(2\phi_r)+\ (J_1(r\xi)+J_3(r\xi))\xi M(\xi)\Delta(\xi)\sin(\phi_r-\phi_{\hat{\mathbf{Q}}_{\mathbf{H}}})\sin(2\phi_r)]\}+$$
$$\int_0^\infty d\xi\xi\sin(\omega_\xi t)\left\{\frac{J_0(r\xi)\xi M(\xi)}{2}\left(1+\frac{\Delta(\xi)}{2}\right)\cos(\phi_{\hat{\mathbf{Q}}_{\mathbf{H}}})+\frac{J_4(r\xi)\xi M(\xi)\Delta(\xi)}{4}\cos(\phi_{\hat{\mathbf{Q}}_{\mathbf{H}}}-4\phi_r)\right.$$
$$\left.-\ \frac{J_2(r\xi)\xi M(\xi)}{2}(1+\frac{\Delta(\xi)}{2})\cos(\phi_{\hat{\mathbf{Q}}_{\mathbf{H}}}-2\phi_r)-\frac{J_2(r\xi)\xi M(\xi)\Delta(\xi)}{4}\cos(\phi_{\hat{\mathbf{Q}}_{\mathbf{H}}}+2\phi_r)\right\} \tag{A54}$$

and

$$C_{\hat{\mathbf{Q}}_{\mathbf{H}}}(\mathbf{r},t)=\int_0^\infty d\xi\xi\sin(\omega_\xi t)\left\{\frac{J_5(r\xi)M(\xi)\Delta(\xi)}{8}\cos(2\phi_{\hat{\mathbf{Q}}_{\mathbf{H}}}-5\phi_r)-\frac{J_3(r\xi)M(\xi)(1-0.5\Delta(\xi))}{4}\cos(2\phi_{\hat{\mathbf{Q}}_{\mathbf{H}}}-3\phi_r)+\right.$$
$$\frac{J_1(r\xi)M(\xi)(1+0.5\Delta(\xi))}{4}\cos(\phi_r)+\frac{J_1(r\xi)M(\xi)(1+\Delta(\xi))}{4}\cos(2\phi_{\hat{\mathbf{Q}}_{\mathbf{H}}})\cos(\phi_r)-\frac{J_3(r\xi)M(\xi)\Delta(\xi)}{4}\cos(3\phi_r)+$$
$$\left.\frac{J_1(r\xi)M(\xi)}{4}\sin(2\phi_{\hat{\mathbf{Q}}_{\mathbf{H}}})\sin(\phi_r)\right\}. \tag{A55}$$

Acknowledgments
The present work was motivated by the study funded under ESA's General Study Program, "Feasibility Investigation of Global Ocean Surface Current Mapping using ERS, MetOp and QuikScat Wind Scatterometer," AO/1–6303/09/NL/AF. The authors wish to thank Alexis Mouche and Bertrand Chapron, IFREMER, for the provision of the empirical Geophysical model function CDOP and the data used in Figure 8 (alexis.mouche@ifremer.fr). The authors thank also Paul Hwang, NRL, for the provision of the wave height spectrum used in Figure 4 (paul.hwang@nrl.navy.mil), and Alexander Voronovich, NOAA, for the useful feedback on the SSA2 implementation. Special thanks go to William J. Plant (plant@apl.washington.edu), the University of Washington, for the provision of the data collected during the SAXON-FPN campaign, available at the following ftp site: ftp://ftp.apl.washington.edu/incoming/plant/Historical_Data/. Chung-Chi Lin, ESA/ESTEC, is also thanked for the useful advises throughout the entire course of the study.

References

Apel, J. R. (1994), An improved model of the ocean surface wave vector spectrum and its effects on radar backscatter, *J. Geophys. Res.*, *99*(C8), 16,269–16,291.

Barrick, D. E., and B. L. Weber (1977), On the nonlinear theory for gravity waves on the ocean's surface, Part II: Interpretation and applications, *J. Phys. Oceanogr.*, *7*(1), 11–21.

Bass, F. G., I. M. Fuks, A. E. Kalmykov, I. E. Ostrovsky, and A. D. Rosenberg (1968), Very high frequency radiowave scattering by a disturbed sea surface Part I: Scattering from a slightly disturbed boundary, *IEEE Trans. Antennas Propag.*, *16*(5), 554–559.

Beckmann, P., and A. Spizzichino (1987), *The Scattering of Electromagnetic Waves From Rough Surfaces*, Artech House, Norwood, Mass.

Chapron, B., F. Collard, and F. Ardhuin (2003), Satellite SAR sea surface Doppler measurements, in *Proceedings of 2nd Workshop on Coastal and Marine Application of SAR, Eur. Space Agency Spec. Publ., ESA SP-565*, pp. 133–139, ESA Publ., Svalbard, Norway.

Chapron, B., F. Collard, and F. Ardhuin (2005), Direct measurements of ocean surface velocity from space: Interpretation and validation, *J. Geophys. Res.*, *110*, C07008, doi:10.1029/2004JC002809.

Coleman, T. F., and Y. Li (1996), An interior trust region approach for nonlinear minimization subject to bounds, *SIAM J. Optim.*, *6*, 418–445.

Cox, C., and W. Munk (1954), Statistics from the sea surface derived from the sun glitter, *J. Mar. Res.*, *13*, 198–227.

Creamer, D. B., F. Henyey, R. Schult, and J. Wright (1989), Improved linear representation of ocean surface waves, *J. Fluid Mech.*, *205*, 135–161.

Donelan, M. A., and W. J. P. Pierson (1987), Radar scattering and equilibrium ranges in wind-generated waves with application to scatterometry, *J. Geophys. Res.*, *92*(C5), 4971–5029.

Elfouhaily, T., B. Chapron, K. Katsaros, and D. Vandemark (1997), A unified directional spectrum for long and short wind-driven waves, *J. Geophys. Res.*, *102*(C7), 15,781–15,796.

Elfouhaily, T., D. Thompson, D. Vandemark, and B. Chapron (1999), Weakly nonlinear theory and sea state bias estimation, *J. Geophys. Res.*, *104*(C4), 7641–7647.

Elfouhaily, T., S. Guignard, R. Awadallah, and D. R. Thompson (2003), Local and nonlocal curvature approximation: A new asymptotic theory for wave scattering, *Waves Random Media*, *13*(4), 321–338.

Fabry, P., et al. (2013), Feasibility study of sea surface currents measurements with Doppler scatterometers, *Proceeding of ESA Living Planet Symposium*, edited by L. Ouwehand, Eur. Space Agency, Edinburgh, U. K.

Fois, F., P. Hoogeboom, F. Le Chevalier, and A. Stoffelen (2014a), An investigation on sea surface wave spectra and approximate scattering theories, in *Geoscience and Remote Sensing Symposium (IGARSS)*, pp. 4366–4369, IEEE.

Fois, F., P. Hoogeboom, F. Le Chevalier, and A. Stoffelen (2014b), Future ocean scatterometry at very strong winds, in *Geoscience and Remote Sensing Symposium (IGARSS)*, pp. 3886–3889, IEEE.

Forget, P., M. Saillard, and P. Broche (2006), Observations of the sea surface by coherent L band radar at low grazing angles in a nearshore environment, *J. Geophys. Res.*, *111*, C09015, doi:10.1029/2005JC002900.

Fung, A., and K. Lee (1982), A semi-empirical sea-spectrum model for scattering coefficient estimation, *IEEE J. Oceanic Eng.*, *7*(4), 166–176.

Hasselmann, K. (1962), On the nonlinear energy transfer in a gravity-wave spectrum Part 1. General theory, *J. Fluid Mech.*, *12*, 481–500.

Hayslip, A. R., J. T. Johnson, and G. R. Baker (2003), Further numerical studies of backscattering from time-evolving nonlinear sea surfaces, *IEEE Trans. Geosci. Remote Sens.*, *41*(10), 2287–2293.

Hwang, P. A., B. Zhang, J. V. Toporkov, and W. Perrie (2010), Comparison of composite Bragg theory and quad-polarization radar backscatter from RADARSAT-2: With applications to wave breaking and high wind retrieval, *J. Geophys. Res.*, *115*, C08019, doi:10.1029/2009JC005995.

Hwang, P. A., D. M. Burrage, D. W. Wang, and J. C. Wesson (2011), An advanced roughness spectrum for computing microwave L-band emissivity in sea surface salinity retrieval, *IEEE Trans. Geosci. Remote Sens.*, *8*(3), 547–551.

Jähne, B., and K. S. Riemer (1990), Two-dimensional wave number spectra of small-scale water surface waves, *J. Geophys. Res.*, *95*(C7), 11,531–11,546.

Johannessen, J. A., B. Chapron, F. Collard, V. Kudryavtsev, A. Mouche, D. Akimov, and K.-F. Dagestad (2008), Direct ocean surface velocity measurements from space: Improved quantitative interpretation of Envisat ASAR observations, *Geophys. Res. Lett.*, *35*, L22608, doi:10.1029/2008GL035709.

Johnson, J. T., J. V. Toporkov, and G. S. Brown (2001), A numerical study of backscattering from time-evolving sea surfaces: Comparison of hydrodynamic models, *IEEE Trans. Geosci. Remote Sens.*, *39*(11), 2411–2420.

Kudryavtsev, V. N., V. K. Makin, and B. Chapron (1999), Coupled sea surface-atmosphere model: 2. Spectrum of short wind waves, *J. Geophys. Res.*, *104*(C4), 7625–7639.

Lee, P. H. Y., J. D. Barter, K. L. Beach, C. L. Hindman, B. M. Lake, H. Rungaldier, J. C. Shelton, A. B. Williams, R. Yee, and H. C. Yuen (1995), X band microwave backscattering from ocean waves, *J. Geophys. Res.*, *100*(C2), 2591–2611, doi:10.1029/94JC02741.

Lee, P. H. Y., J. D. Barter, E. Caponi, M. Caponi, C. L. Hindman, B. M. Lake, and H. Rungaldier (1996), Wind-speed dependence of small-grazing-angle microwave backscatter from sea surfaces, *IEEE Trans. Antennas Propag.*, *44*(3), 333–340, doi:10.1109/8.486302.

Li, X., and X. Xu (2011), Scattering and Doppler spectral analysis for two-dimensional linear and nonlinear sea surfaces, *IEEE Trans. Geosci. Remote Sens.*, *49*(2), 603–611.

Longuet-Higgins, M. S. (1963), The effect of nonlinearities on statistical distributions in the theory of sea waves, *J. Fluid Mech.*, *17*(03), 459–480.

Mouche, A. A., B. Chapron, N. Reul, and F. Collard (2008), Predicted Doppler shifts induced by ocean surface wave displacements using asymptotic electromagnetic wave scattering theories, *Waves Random Complex Media*, *18*(1), 185–196.

Mouche, A. A., F. Collard, B. Chapron, K. Dagestad, G. Guitton, J. A. Johannessen, V. Kerbaol, and M. W. Hansen (2012), On the use of Doppler Shift for sea surface wind retrieval from SAR, *IEEE Trans. Geosci. Remote Sens.*, *50*(7), 2901–2909.

Nie, D., M. Zhang, X.-P. Geng, and P. Zhou (2012), Investigation on Doppler spectral characteristics of electromagnetic backscattered echoes from dynamic nonlinear surfaces of finite-depth sea, *Prog. Electromagn. Res.*, *130*, 169–186.

Nouguier, F., C. A. Guèrin, and B. Chapron (2009), Choppy wave model for nonlinear gravity waves, *J. Geophys. Res.*, *114*, C09012, doi:10.1029/2008JC004984.

Nouguier, F., C. A. Guèrin, and B. Chapron (2010), Scattering from nonlinear gravity waves: The 'Choppy Wave' Model, *IEEE Trans. Geosci. Remote Sens.*, *48*(12), 4184–4192.

Nouguier, F., A. Guèrin, and G. Soriano (2011), Analytical techniques for the Doppler signature of sea surfaces in the microwave regime II: Nonlinear surfaces, *IEEE Trans. Geosci. Remote Sens.*, *49*(12), 4920–4927.

Papoulis, A. (1965), *Probability Random Variables and Stochastic Processes*, pp. 153–162, McGraw-Hill, Boston, Mass.

Pierson, W. J., and L. Moskowitz (1964), A proposed spectral form for fully developed wind sea based on the similarity theory of S. A. Kitaigorodskii, *J. Geophys. Res.*, *69*(24), 5181–5190.

Plant, W. J. (1997), A model for microwave Doppler sea return at high incidence angles: Bragg scattering from bound, tilted waves, *J. Geophys. Res.*, *102*(C9), 21,131–21,146, doi:10.1029/97JC01225.

Plant, W. J. (2002), A stochastic, multiscale model of microwave backscatter from the ocean, *J. Geophys. Res.*, *107*(C9), 3120, doi:10.1029/2001JC000909.

Plant, W. J., and W. Alpers (1994), An introduction to SAXON-FPN, *J. Geophys. Res.*, *99*(C5), 9699–9703.

Plant, W. J., W. C. Keller, R. A. Petitt, and E. A. Terray (1994), The dependence of microwave backscatter from the sea on illuminated area: Correlation times and lengths, *J. Geophys. Res.*, *99*(C5), 9705–9723.

Plant, W. J., W. C. Keller, V. Hesany, T. Hara, E. Bock, and M. A. Donelan (1999), Bound waves and Bragg scattering in a wind-wave tank, *J. Geophys. Res.*, *104*(C2), 3243–3263, doi:10.1029/1998JC900061.

Rino, C. L., T. L. Crystal, A. K. Koide, H. D. Ngo, and H. Guthart (1991), Numerical simulation of backscattering from linear and nonlinear ocean surface realizations, *Radio Sci.*, *26*(1), 51–71.

Rodriguez, E., M. M. Flexas, D. Menemenlis, D. Perkovic-Martin, and A. F. Thompson (2014), DopplerScat: A pencil-beam scatterometer and surface current instrument, in *International Ocean Vector Wind Science Team Meeting*, Center for Ocean-Atmospheric Prediction Studies, Brest, France.

Romeiser, R., and D. R. Thompson (2000), Numerical study on the along-track interferometric radar imaging mechanism of oceanic surface currents, *IEEE Trans. Geosci. Remote Sens.*, *38*(1), 446–458.

Soriano, G., M. Joelson, and M. Saillard (2006), Doppler spectra from a two-dimensional ocean surface at L-band, *IEEE Trans. Geosci. Remote Sens.*, *44*(9), 2430–2437.

Stoffelen, A., et al. (2013), Research and development in Europe on global application of the OceanSat-2 scatterometer winds, *Document External Project: 2013, NWP SAF Rep. NWPSAF-KN-TR-022, OSI SAF Rep. SAF/OSI/CDOP2/KNMI/TEC/RP/196*, Koninklijk Nederlands Meteorologisch Instituut (KNMI), de Bilt, Netherlands.

Thompson, D. R. (1989), Calculation of microwave Doppler spectra from the ocean surface with a time-dependent composite model, in *Radar Scattering From Modulated Wind Waves*, edited by G. J. Komen and W. A. Oost, pp. 27–40, Kluwer Acad.

Toporkov, J. V., and G. S. Brown (2000), Numerical simulations of scattering from time-varying, randomly rough surfaces, *IEEE Trans. Geophys. Remote Sens.*, *38*, 1616–1624.

Toporkov, J. V., and M. A. Sletten (2007), Statistical properties of low-grazing range-resolved sea surface backscatter generated through two-dimensional direct numerical simulations, *IEEE Trans. Geosci. Remote Sens.*, *45*(5), 1181–1197.

Ulaby, F. T., R. K. Moore, A. K. Fung (1990), *Microwave Remote Sensing: Active and Passive: Radar Remote Sensing and Surface Scattering and Emission Theory*, vol. II, Artech House, Norwood, Mass.

Valenzuela, G. R., and M. B. Laing (1970), Study of Doppler spectra of radar sea echo, *J. Geophys. Res.*, *75*(3), 551–563.

Van Zadelhoff, G.-J., A. Stoffelen, P. W. Vachon, J. Wolfe, J. Horstmann, and M. Belmonte Rivas (2013), Scatterometer hurricane wind-speed retrievals using cross-polarization, *Atmos. Meas. Tech. Discuss.*, *6*, 7945–7984.

Voronovich, A. (1994), Small-slope approximation for electromagnetic wave scattering at a rough interface of two dielectric half-spaces, *Waves Random Complex Media*, *4*(3), 337–367.

Voronovich, A. G., and V. U. Zavorotny (2001), Theoretical model for scattering of radar signals in Ku- and C-bands from a rough sea surface with breaking waves, *Waves Random Media*, *11*, 247–269.

West, B. J., K. A. Brueckner, R. S. Janda, D. M. Milder, and R. L. Milton (1987), A new numerical method for surface hydrodynamics, *J. Geophys. Res.*, *92*(C11), 11,803–11,824.

Wright, J. W. (1968), A new model for sea clutter, *IEEE Trans. Antennas Propag.*, *16*(2), 217–223.

Zavorotny, V. U., and A. G. Voronovich (1998), Two-scale model and ocean radar Doppler spectra at moderate-and low-grazing angles, *IEEE Trans. Antennas Propag.*, *46*(1), 84–92.